A microphysical model of rock friction and the brittle-ductile transition controlled by dislocation glide and backstress evolution

Christopher A. Thom[1,2,*], Lars N. Hansen[3], David L. Goldsby[4] & Emily E. Brodsky[2]

[1] Department of Earth Sciences, University of Oxford, Oxford, OX1 3AN, U.K.

[2] Department of Earth & Planetary Sciences, University of California, Santa Cruz, California, 95064, U.S.A.

[3] Department of Earth and Environmental Sciences, University of Minnesota-Twin Cities, Minneapolis, Minnesota, 55455, U.S.A.

[4] Department of Earth and Environmental Science, University of Pennsylvania, Philadelphia, Pennsylvania, 19104, U.S.A.

[*] Corresponding author

Abstract

Rate- and state-friction is an empirical framework that describes the complex velocity-, time-, and slip-dependent phenomena observed during frictional sliding of rocks and gouge in the laboratory. Despite its widespread use in earthquake nucleation and recurrence models, our understanding of rate- and state-friction, particularly its time- and/or slip-dependence, is still largely empirical, limiting our confidence in extrapolating laboratory behavior to the seismogenic zone. While many microphysical models have been proposed over the past few decades, none have explicitly incorporated the effects of strain hardening, anelasticity, or transient viscous rheology. Here we present a new model of rock friction that incorporates these phenomena directly from the microphysical behavior of lattice dislocations. This model of rock friction exhibits the same logarithmic dependence on sliding velocity (strain rate) as rate- and state-friction and predicts a dependence on the internal backstress caused by long-range interactions among geometrically necessary dislocations. Changes in the backstress evolve exponentially with plastic strain of asperities and are dependent on both the current backstress and previous deformation, which give rise to phenomena consistent with interpretations of the 'critical slip distance,' 'memory effect,' and 'state variable' of rate- and state-friction. Fault stability in this model is controlled by the evolution of backstress and temperature. We provide several analytical predictions for RSF-like behavior and the 'brittle-ductile' transition based on

microphysical mechanisms and measurable parameters such as the geometrically necessary dislocation density and strain-dependent hardening modulus.

Plain Language Summary

For decades, the friction coefficient between two rocks has been known to depend on the time in contact and previous sliding. This framework, called rate- and state-friction, has been notoriously difficult to explain using physical arguments, despite its utility in understanding the earthquake cycle. Conventional interpretations of rock friction often invoke the occurrence of permanent deformation at microscopic scales, but an explanation of the 'memory-dependence' (the dependence on previous sliding) has remained elusive. In this paper, we consider the defects in the material (dislocations) that are generated and stored by permanent deformation. Over time, a rock accumulates dislocations which results in an apparent memory effect. We predict the abundance and interactions between these dislocations with small changes in the deformation of the surfaces. Specifically, we take into account the interactions between these defects, which strengthens the material, ultimately leading to a friction coefficient that depends on time and previous deformation, like in rate- and state-friction. From our theory, we make quantitative predictions about the frictional behavior of rocks in the laboratory and in nature based on measurable material properties.

Keywords

Friction; plasticity; strain hardening; backstress

Key points

- We derive rate- and state-frictional behavior by considering dislocation glide and the evolution of interactions between dislocations.
- Our 'state evolution' law acts similarly to the slowness and slip laws under different assumptions and testing conditions.
- We predict the brittle-ductile transition with a microphysical framework that depends on temperature and backstress evolution.

1. Introduction

Rate- and state-friction (RSF) has been used for decades to describe the frictional sliding of rocks and gouge in the laboratory (Marone, 1998; Scholz, 2002). Although it is empirical in nature, it has been applied successfully to explain phenomena in the context of both seismic slip (e.g., Dieterich, 1992; Lapusta et al., 2000; Rubin & Ampuero, 2005; Ampuero & Rubin, 2008) and slow slip events (e.g., Shibazaki & Iio, 2003; Rubin 2008; Ikari et al., 2013; Kaproth & Marone, 2013; Hawthorne & Rubin, 2013a; Hawthorne & Rubin, 2013b; Leeman et al., 2016; Im et al., 2020). Because of its widespread use and importance in interpreting the emerging richness of fault slip behaviors, understanding the physical mechanism(s) that give(s) rise to RSF in the laboratory and in nature is a critical outstanding goal in geophysics.

Decades of work to describe the microphysics of RSF for intact rocks and gouge, typically using a thermally activated rheology, have led to an improved understanding (e.g., Brechet & Estrin; 1994; Estrin & Brechet, 1996; Rice et al., 2001; Bos & Spiers, 2002; Niemeijer & Spiers, 2007; Putelat et al., 2010; Bar-Sinai et al., 2014; Hatano, 2015; Noda & Takahashi, 2016; Ikari et al., 2016; Chen et al., 2017; Molinari & Perfettini, 2017; Perfettini & Molinari, 2017; Tian et al., 2018; van den Ende et al., 2018; Aharonov & Scholz, 2018; 2019; Barbot, 2019; Verberne et al., 2020; Chen et al., 2020), but significant uncertainties still remain when extrapolating beyond the relatively limited set of conditions tested in the laboratory. In particular, frictional behavior near the brittle-ductile transition has remained poorly constrained, despite some high-temperature laboratory experiments (Stesky, 1978; Blanpied et al., 1991; Chester & Higgs, 1992; Chester, 1994; Blanpied et al., 1995; 1998; Boettcher et al., 2007; King & Marone, 2012). In addition, because RSF describes both steady-state and transient frictional behavior, our limited understanding of transient rheology in geologic materials has hindered further theoretical development.

Here, we utilize classical Bowden & Tabor (1950) friction theory and elastoplastic contact mechanics like many previous authors. However, motivated by recent advances in the understanding of the microphysics of deformation in olivine (Hansen et al., 2019; Wallis et al., 2020; Hansen et al., 2021; Thom et al., 2021; Breithaupt, 2021), our model explicitly incorporates strain hardening and transient deformation, which have not been previously considered for rock friction. We account for these effects in our model by utilizing the indentation hardness at the appropriate length scale of asperities and the plasticity flow law of

Hansen et al. (2019), which explicitly includes nominally temperature-independent strain hardening, which gives rise to an internal 'backstress' that resists further deformation. A schematic picture of this model is presented in Figure 1, where we demonstrate that the real contact area is determined by the indentation hardness, while the shear strength of an average asperity is determined by a combination of dislocation glide and backstress (which together result in 'low-temperature plasticity') in the deforming volume. Backstress is expected to increase frictional resistance by pre-hardening asperities, as demonstrated schematically in Figure 1. Furthermore, accounting for this backstress and its evolution results in a memory, or state, dependence that is different from other proposed mechanisms.

We will first briefly review the empirical equations of RSF and summarize the salient laboratory observations that provide the basis for these formulations in Section 2. The low-temperature plasticity and strain hardening constitutive laws will be introduced in Section 3, followed by the full description of our model in Section 4. We provide testable laboratory hypotheses and outline the implications for lithospheric strength and the brittle-ductile transition in Section 5.

2. Rate- and state-friction (RSF)

2.1 Basic equations and observations

The frictional sliding of rocks and fault gouge is typically described using the framework of rate- and state-friction (RSF), which is a set of empirical equations that capture the complex velocity-, time-, and displacement-dependent friction coefficient (Dieterich, 1972; Dieterich, 1978; Ruina, 1983; Marone, 1998; Scholz, 2002). In this model, the current friction coefficient μ is a function of current sliding velocity V and state variable θ, given by

$$\mu = \mu_0 + a \ln\left(\frac{V}{V_0}\right) + b \ln\left(\frac{V_0\theta}{D_c}\right), \qquad \text{Eq. 1}$$

where μ_0 is the steady-state friction coefficient at reference velocity V_0. The unitless coefficients a and b describe the magnitude of two competing effects, known as the 'direct effect' and the 'evolution effect,' which will be discussed in more detail below.

106 The state variable θ has units of time, and D_c is referred to as the 'critical slip distance,' or the
107 'memory distance,' which is a length scale related to the distance the fault needs to slip to reach the new
108 steady-state upon a change in the 'state variable.' The 'critical slip distance' is often interpreted to be the
109 average (or maximum) size of microscopic contact junctions on the surface, called asperities, which are
110 inferred to deform plastically (Dieterich & Kilgore, 1994; 1996). The most common empirical descriptions
111 of *state evolution*, or how the state variable changes with time (t) and slip are the *slowness law* (also known
112 as the *aging law*) (Dieterich, 1978) and the *slip law* (Ruina, 1983), given by

113 $$\frac{d\theta}{dt} = 1 - \frac{V\theta}{D_c} \qquad \text{Eq. 2}$$

114 and

115 $$\frac{d\theta}{dt} = -\frac{V\theta}{D_c}\ln\left(\frac{V\theta}{D_c}\right), \qquad \text{Eq. 3}$$

116 respectively. A key difference exists between these two formulations, which has major implications for the
117 frictional evolution and nucleation behavior of faults. The state variable in the slowness law (Eq. 2)
118 increases with time at zero sliding velocity, whereas the slip law (Eq. 3) requires slip for the 'state' to
119 evolve. The slip law has generally become more favored in recent years (e.g., Bhattacharya et al., 2015;
120 2017), but despite decades of experiments and theoretical considerations, neither state evolution law can
121 explain all of the available data or observations. Hybrid state evolution laws that combine aspects of both
122 time- and slip-dependent laws also cannot reproduce all of the laboratory observations (Perrin et al., 1995;
123 Kato & Tullis, 2001; Nagata et al., 2012).

124 The 'direct' and 'evolution effect' are most easily observed in a 'velocity-step' friction test, which
125 begins with a laboratory fault sheared at velocity V_0, yielding a steady-state value of friction, μ_0. Upon a
126 step up (or down) to the new velocity V, friction increases (decreases) abruptly by a factor of a (the 'direct
127 effect') and then decays (grows) exponentially over a characteristic slip distance (D_c) by a factor b to a new
128 steady-state level (the 'evolution effect') due to 'state evolution'. Assuming at steady-state that $V = \frac{D_c}{\theta}$,
129 one can write

$$\mu = \mu_0 + (a - b)\ln\left(\frac{V}{V_0}\right) \quad \text{Eq. 4}$$

to describe fault stability. A necessary requirement for earthquake nucleation is that the relative magnitudes of a and b yield a decrease in friction with increasing V (i.e., a-b < 0), known as velocity-weakening friction (Rice, 1983; Rice & Ruina, 1983; Gu et al., 1984). This behavior is distinct from the typical *increase* in material strength with increasing deformation rate.

The 'evolution effect' is also studied indirectly in 'slide-hold-slide' (SHS) tests. After steady-state sliding at some velocity, the load-point velocity is held at zero for a set period of time, followed by resumption of sliding at the pre-hold velocity. The shear strength of the interface increases during the hold, such that friction in excess of the steady-state value must be overcome upon re-loading. Stress relaxation, lateral slip, and fault-normal creep of asperities on the interface occur during the hold, making it difficult to distinguish the correct state evolution equation to use (i.e., time- or slip-dependent). Once sliding re-initiates and the peak friction is reached, friction drops to the previous steady-state value. The value of the change in friction, or alternatively the peak friction, increases approximately linearly with the logarithm of time held in quasi-stationary contact (Dieterich, 1972).

2.2 Interpretations of RSF phenomena

The direct effect is attributed to thermally-activated processes (e.g., Rice et al., 2001; Nakatani, 2001; Hatano, 2015; Tian et al., 2018) and thus modeled as having a logarithmic dependence on velocity (Eq. 1). This dependence is seen in experiments ranging from investigations of atomic stick-slip in atomic-force microscopy (Liu et al., 2015) to the macroscopic frictional behavior of rocks (Marone, 1998). The physical origin of the direct effect is typically attributed to thermally-activated slip via either shear creep or pure interfacial slip (Rice et al., 2001). A statically-loaded frictional interface consists of asperities such that sliding requires overcoming energy barriers. The applied shear force is thus assisted by thermal energy. The slower the slip rate, the more time thermal vibrations have to assist in overcoming the energy barrier, yielding increasing friction with increasing velocity. In terms of bulk deformation, one might also derive the logarithmic dependence from the strain rate depending exponentially on the differential stress, assuming

some layer thickness over which sliding is accommodated (e.g., Ruina, 1981; Sleep, 2006), as in most constitutive laws for low-temperature plasticity. For example, the magnitude of the direct effect in olivine friction experiments is in agreement with that predicted from the rate-dependence of low-temperature plasticity flow laws (Boettcher et al., 2007; King & Marone, 2012).

In contrast, the physical basis for the evolution effect remains uncertain. The conventional view states that changes in friction due to the 'evolution effect' arise from changes in the real contact area (e.g., Dieterich & Kilgore, 1994; Boettcher et al., 2007). However, observations from friction experiments on rocks and analogue materials indicate that friction and contact area are not well correlated during the transient phase of sliding. For example, in the experiments performed by Dieterich and Kilgore (1994), friction varies in velocity-step experiments in association with changes in the measured contact area. However, the contact area varies in a stepwise fashion at velocity steps, whereas friction is observed to evolve more slowly than a step function (see their Fig. 8). Similar conclusions have been reached in more recent rock friction experiments wherein acoustic transmissivity through the frictional interface, a proxy for contact area, is measured simultaneously with friction (Nagata et al., 2008; Kilgore et al., 2012; Nagata et al., 2014; Kilgore et al., 2017). Although the machine is resonating slightly in their velocity steps, Nagata et al. (2014) presented data in which the contact area (measured by two separate methods) instantaneously decreases upon an increase in the sliding velocity, but then increases slightly over time to a new steady-state value. The shear stress appears to evolve over a similar timescale, but it is clearly not synchronized directly with the contact area. Thus, a one-to-one correlation between contact area and shear stress cannot be inferred. Additionally, in the normal stress-stepping experiments of Kilgore et al. (2012) and Kilgore et al. (2017), contact area changes rapidly, while additional time (or slip) is required for friction to evolve completely after a step. Clearly, friction and contact area are related, but changes in contact area alone cannot explain changes in friction. This is also the conclusion of nanoindentation tests on quartz at low and high humidity, which sought to test the effect of water on the room temperature creep behavior of asperities (Thom et al., 2018).

3. Recent advances in low-temperature plasticity and transient rheology

Recent experiments have improved our physical understanding of low-temperature plasticity, strain hardening, and transient deformation in geologic materials. Hansen et al. (2019) performed cyclic deformation tests in a D-DIA apparatus wherein single crystal and polycrystalline olivine samples were deformed alternately in compression and extension at room temperature and elevated temperature (873 K or less). When initially deformed in compression, samples with different grain sizes and single crystal orientations yielded plastically at stresses of 1.8 to 4.1 GPa, with the yield stress increasing with decreasing grain size in a manner consistent with that suggested by Kumamoto et al. (2017). Importantly, after initially yielding in compression, all samples strain hardened by an additional 1.5 to 2 GPa before reaching a steady-state flow stress after several percent plastic strain. Upon reversing the sense of deformation to extension, the same samples plastically yielded in the opposite direction at stresses smaller than the initial yield stress due to the addition of a backstress, which is an internal stress that is directed opposite to the initial applied stress (Dieter, 1986 and references therein). In the Hansen et al. (2019) experiments, one sample even yielded in extension while still under a small positive differential stress (i.e., a compressional stress), implying that the backstress was larger than the initial yield stress (see data for San389bottom in Hansen et al., 2019). This mechanical behavior represents 'reverse flow' as the sample is unloaded from a compressional stress to zero differential stress. At sufficiently rapid unloading rates, this deformation will appear to be anelastic, meaning the deformation is both recoverable and time-dependent. This behavior has also been noted in room-temperature nanoindentation experiments on the same material (Thom et al., 2021).

Backstresses arise due to long-range elastic interactions among geometrically necessary dislocations (GNDs), which are dislocations of the same sign required to maintain compatibility at grain boundaries or to allow curvature of the crystal lattice (e.g., Ashby, 1970). If the strain field accommodating plastic deformation is non-uniform (i.e., a strain gradient exists), GNDs must exist to accommodate incompatibilities (Ashby, 1970). During strain hardening, the density of GNDs increases until the rate of dislocation generation is balanced by recovery mechanisms such as dislocation climb, cross-slip, or annihilation. This increase in GND density (alternatively, the decrease in average GND spacing) results in an increasing backstress described by the Taylor equation (Taylor, 1934),

$$\sigma_{\mathrm{b}} = \alpha G b_{\mathrm{v}} \sqrt{\rho_{\mathrm{GND}}}, \qquad \text{Eq. 5}$$

where σ_{b} is the backstress, α is a constant (approximately 3 in many geological materials as demonstrated by Thom et al., 2021), *G* is the shear modulus, b_{v} is the Burgers vector, and ρ_{GND} is the density of geometrically necessary dislocations. Subsequent investigations of the microstructures of the samples in Hansen et al. (2019) revealed alternating bands of elevated GND densities with spacings of 1-100 μm and residual stress heterogeneity of up to +/- 3 GPa, supporting the assertion that the build up of GNDs and long-range elastic interactions among them gives rise to the backstress (Wallis et al., 2020; 2021).

All studies using plastic rheology for rock friction, and most other studies of plasticity in geological materials utilize a flow law of the form

$$\dot{\varepsilon}_{\mathrm{LTP}} = A\sigma^{n}\exp\left[-\frac{E+PV^{*}}{RT}\left(1-\left(\frac{\sigma}{\sigma_{\mathrm{P}}(P)}\right)^{p}\right)^{q}\right], \qquad \text{Eq. 6}$$

where $\dot{\varepsilon}_{\mathrm{LTP}}$ is the low-temperature plasticity strain rate, *A* is a material parameter, σ is the differential stress, *n* is the stress exponent, *E* is the activation energy, *P* is the confining pressure, *V** is the activation volume, *R* is the gas constant, *T* is the absolute temperature, *p* and *q* are constants, and σ_{p} is the Peierls stress. The stress exponent, *n,* in this formulation typically has a value of 0 or 2 in studies of olivine (see review in Proietti et al., 2016), and the constants *p* and *q* can take on values between 0.5 and 2 depending on the assumed shape of energy barriers opposing dislocation glide (Kocks, 1976). The values *p* and *q* are notoriously difficult to constrain, as demonstrated by Jain et al. (2017). For box shaped potentials caused by local interactions between evenly spaced obstacles, Frost & Ashby (1982) suggest *p* and *q* should both be equal to 1, which are the values assumed in the work of Hansen et al. (2019). The Peierls stress σ_{p}, sometimes loosely referred to as 'lattice friction,' is the inherent resistance to dislocation glide from the crystal lattice at 0 K. The Peierls stress is usually assumed to have a negligible dependence on pressure, but a pressure term like that shown in Eq. 6 is sometimes included (e.g., Kawazoe et al., 2009; Proietti et al., 2016).

Because low-temperature plasticity flow laws are typically calibrated to the yield stress or flow stress, they do not explicitly incorporate the transient effects of strain hardening. Hansen et al. (2019)

presented a model with a different microphysical and mathematical basis to account for dislocation-induced backstresses. A slightly modified version of a plasticity flow law was presented in Hansen et al. (2021), who wrote the strain rate as

$$\dot{\varepsilon}_{\mathrm{LTP}} = A\rho \exp\left(-\frac{E}{RT}\right) \sinh\left(\frac{E}{RT}\frac{\sigma - \sigma_{\mathrm{b}}}{\sigma_{\mathrm{P}}}\right), \qquad \text{Eq. 7}$$

where ρ is the dislocation density and σ_{b} is the backstress. The quantity $\sigma - \sigma_{\mathrm{b}}$ is defined as the 'effective stress,' which controls the rate of dislocation glide. Note that this effective stress is not equivalent to the term of the same name commonly used in studies related to the effects of pore pressure in rocks. The use of the hyperbolic sine function here allows for both positive and negative stresses to be considered (and thus both positive and negative strain rates). Hansen et al. (2019) initially constrained the values of these flow law parameters for olivine, and Hansen et al. (2021) re-calibrated the flow law using available high temperature data for the same deformation mechanism (i.e., dislocation glide). This formulation has not yet been applied to other geological materials, but values could be derived with a focused study on important crustal minerals.

We can rewrite Eq. 7 as

$$\sigma = \frac{RT\sigma_{\mathrm{P}}}{E} \sinh^{-1}\left[\frac{\dot{\varepsilon}_{\mathrm{LTP}}}{A\rho} \exp\left(\frac{E}{RT}\right)\right] + \sigma_{\mathrm{b}} \qquad \text{Eq. 8}$$

to evaluate the axial differential stress felt by the sample (i.e., the applied stress). This equation highlights that the differential stress is the sum of two terms. The first effectively describes the 'yield stress,' which is thermally activated and a function of the strain rate. The second term is simply the 'backstress,' which opposes further deformation and results from the interactions among GNDs (see Eq. 5). Hansen et al. (2019) found the backstress to be independent of both grain size and temperature over the range tested. Backstress only evolves as a function of GND density, which Hansen et al. (2019) simply parameterized as a function of strain using

$$\frac{d\sigma_{\mathrm{b}}}{d\varepsilon_{\mathrm{p}}} = \gamma[\sigma_{\mathrm{b,max}} - \mathrm{sgn}(\dot{\varepsilon_{\mathrm{p}}})\sigma_{\mathrm{b}}], \qquad \text{Eq. 9}$$

where γ is a rate constant, $\sigma_{b,max}$ is the maximum backstress, ε_p is the plastic strain and $\dot{\varepsilon}_p$ is the plastic strain rate. Although Eq. 9 was employed empirically in Hansen et al. (2019), it has a microphysical basis. The product $\gamma\sigma_{b,max}$ is closely related to the dislocation nucleation rate and initial hardening modulus at the yield point (Armstrong & Frederick, 1966; Mecking & Kocks, 1981; Hansen et al., 2021). We can solve Equation 9 analytically as

$$\sigma_b(\varepsilon_p) = \mathrm{sgn}(\dot{\varepsilon}_p)\sigma_{b,max} + (\sigma_{b,0} - \mathrm{sgn}(\dot{\varepsilon}_p)\sigma_{b,max})\exp(-\gamma\varepsilon_p \mathrm{sgn}(\dot{\varepsilon}_p)), \quad \text{Eq. 10}$$

where $\sigma_{b,0}$ is the initial backstress. The plastic strain-rate terms allow for the backstress to be determined as a function of time, and the incorporation of the sign function allows for both positive and negative deformation rates. Equation 10 suggests that when plastic strain is being accrued (in either a positive or negative direction), the backstress evolves in an exponential fashion and is dependent on the initial backstress. We will illustrate in Sections 4 and 5 that Eq. 10 effectively acts as a 'state evolution' law, for which changes in backstress reflect changes in the 'state,' and therefore friction. Interestingly, because backstress evolution is strain-rate dependent, the evolution has a dependence on both time and slip (through a proxy strain dependence), consistent with interpretations of both Eqs. 2 and 3.

4. A microphysical model for rock friction

4.1 Surface roughness and contact mechanics

As a result of surface roughness, only a small percentage of the apparent area of contact between two surfaces is truly in contact (e.g., Greenwood & Williamson, 1966; Bush et al., 1975; Dieterich & Kilgore, 1994; 1996; Persson, 2001; Hyun et al., 2004; Pei et al., 2005; Nagata et al., 2014; Kilgore et al., 2017; Thom et al., 2017), and numerous studies have demonstrated that both natural and laboratory fault surfaces exhibit self-affine fractal surface roughness (e.g., Renard et al., 2006; Candela et al., 2012; Brodsky et al., 2016; Thom et al., 2017; Harbord et al., 2017). Assuming that the mean contact stress on asperities is equal to the indentation hardness, H (in agreement with the results of Thom et al., 2017), the real contact area (A_r) between two self-affine surfaces is given by

$$A_r = \frac{F_n}{H}, \quad \text{Eq. 11}$$

where F_n is the nominal normal force. We note that Thom et al. (2017) demonstrated that indentation hardness was scale-dependent (i.e., smaller indents had higher hardness) in a manner consistent with predictions from Brodsky et al. (2016) based on surface roughness measurements. Several other studies have identified a similar magnitude size effect in the plastic deformation of geologic materials (Kumamoto et al., 2017; Thom et al., 2018; Thom & Goldsby, 2019; Koizumi et al., 2020), suggesting that the real contact area of a surface is indeed controlled by its scale-dependent hardness (Thom et al., 2017). The effect of scale-dependent strength on contact mechanics has been considered theoretically by Persson (2006), but few studies have addressed the problem (Venugopalan et al., 2019; Tiwari et al., 2020). Thus, we will neglect the scale-dependence here and use the hardness at the inferred length scale of asperities, D_c.

4.2 Bowden & Tabor friction with strain hardening

Bowden & Tabor (1950) suggested that

$$F_f = \tau A_r, \quad \text{Eq. 12}$$

where F_f is the average friction force (shear force), and τ is the average shear strength of asperities. Using Eq. 11, we can also write this as

$$F_f = \tau \frac{F_n}{H}. \quad \text{Eq. 13}$$

Dividing both sides of Eq. 13 by the normal force gives

$$\frac{F_f}{F_n} = \mu = \frac{\tau}{H}, \quad \text{Eq. 14}$$

where μ is the friction coefficient. This result is not itself new, as many authors have arrived at a similar formulation, and this result is effectively the same as the original conclusion drawn by Bowden & Tabor (1950) and Dieterich & Kilgore (1994). Subsequently, several authors have attempted to derive rate- and state-frictional behavior by introducing time-dependent hardness (i.e., contact stress), time-dependent contact area (inversely proportional to H, from Eq. 11), time-dependent chemical bonding (Tian et al., 2018), or a constitutive law for low-temperature plasticity into Eq. 14 (e.g., Dieterich & Kilgore, 1994; Boettcher et al., 2007; Aharonov & Scholz, 2018), but none have explicitly incorporated the transient effects

of strain hardening and backstress. We substitute Eq. 8 into Eq. 14, accounting for the fact that $\tau = \sqrt{3}\sigma$, and derive

$$\mu = \frac{\sqrt{3}\left(\frac{RT\sigma_{\mathrm{P}}}{E}\sinh^{-1}\left[\frac{\dot{\varepsilon}}{A\rho}\exp\left(\frac{E}{RT}\right)\right] + \sigma_{\mathrm{b}}\right)}{H}, \qquad \text{Eq. 15}$$

where $\dot{\varepsilon}$ is the sliding strain rate, defined as $\dot{\varepsilon} = \frac{V}{X}$, V is the sliding velocity, and X is some thickness over which deformation is localized, similar to Ruina (1981) and Sleep (2006). We note that the microphysics controlling H are the same as for the shear stress (the numerator of Eq. 15) and can be written as a flow law with the same form (i.e., $H = \sigma_y + \sigma_{\mathrm{b,H}}$, where σ_y is a yield stress and $\sigma_{\mathrm{b,H}}$ is the backstress associated with the indentation hardness). Variations in the hardness arise from small variations in the fault-normal strain rate, and can be considered negligible here because they are much smaller than the sliding strain rate. The form of Eq. 15 already leads to interesting comparisons with rate- and state-friction (RSF). Using the approximation $\sinh^{-1}(x) \approx \ln(2x)$, we immediately recover the logarithmic strain rate (sliding velocity) dependence of friction. An additional microphysically motivated term representing the 'state variable,' here the internal backstress, which is controlled by the GND density in asperities, also contributes to the frictional resistance. Although not obvious at first, these two terms depend on the sliding velocity in an opposite sense, which will be discussed in more detail below.

Although the authors of previous investigations of plasticity note that dislocation density is the microphysical mechanism controlling the backstress (Hansen et al., 2019; Wallis et al., 2020; Thom et al., 2021; Hansen et al., 2021; Breithaupt, 2021), it is not a property that is possible to directly measure during a friction experiment. During steady-state sliding, individual asperities are coming into and out of contact. These asperities may deform elastically or inelastically to produce wear products, and some re-roughnening processes must exist to generate new roughness to maintain topography (Brodsky et al., 2016). Thus, it is likely that some combination of previously deformed and newly formed asperities make up the frictional interface. Small changes in the fault-normal displacement during 'state evolution' should reflect variations in the average local asperity strain (and thus the dislocation density and backstress), while a longer term

trend may reflect generation of wear products. Assuming that the thickness X over which deformation is accommodated is equal to the diameter of the largest plastically deforming asperities (i.e., the deformation is accommodated in a hemisphere, which is the asperity), we can relate the sliding strain rate to the largest asperity size L (which is thought to correspond to the variable D_c), although we do not explicitly make this assumption *a priori*. However, it is an appealing possibility because D_c has been suggested to be a length scale that demarcates the transition from plastic deformation to brittle mechanisms (Candela & Brodsky, 2016), and variations in D_c can be predicted from material properties (Okamoto et al., 2019). Furthermore, as we will demonstrate below, a length scale related to the size of the deforming region emerges naturally from 'strain-gradient plasticity' theory (e.g., Nix & Gao, 1998).

Starting with Eq. 20, we derive the *rate dependence* (i.e., the a value of RSF) of friction by finding the difference between the friction coefficient at a new strain rate $\dot{\varepsilon}_1$ (an e-fold increase) relative to the value at reference strain rate $\dot{\varepsilon}_0$. This derivation only considers the instantaneous strain rate response, which is captured with the typical thermally activated terms. A full derivation is provided in the Appendix, where we show that

$$a \approx \sqrt{3}\frac{RT\sigma_{\mathrm{P}}}{EH}. \qquad \text{Eq. 16}$$

As with previous studies, the a parameter here captures the thermal rate dependence of friction.

We also derive the *state dependence* (i.e., the b value of RSF, which here is controlled by backstress evolution) in a similar manner by using the backstress evolution law (Eq. 10), as detailed in the Appendix. We determine the difference between the final friction coefficient at $\sigma_{\mathrm{b},1}$ and the reference friction coefficient at $\sigma_{\mathrm{b},0}$. This procedure yields

$$b \approx \frac{\sqrt{3}(\sigma_{\mathrm{b,max}} - \sigma_{\mathrm{b},0})\gamma\beta}{H} \qquad \text{Eq. 17}$$

where β is a characteristic strain in the fault-normal direction for an e-fold change in sliding strain rate. While fault-normal strains from changes in shear stress or shear velocity may seem unexpected, it is a well-known phenomenon in soils and anisotropic metals known as non-associated flow, where changes in strain

need not be orthogonal to the changes in stress (e.g., Zienkiewicz et al., 1975 and references therein; Qin & Bassani, 1992; Stoughton & Yoon, 2009; Safaei et al., 2014). This characteristic strain in Eq. 17 may itself be a function of the reference sliding velocity or other material properties, but such speculation is beyond the scope of this manuscript. Another interesting aspect of Eq. 17 is that , a thermal dependence of the *b* value arises through the indentation hardness, despite backstress being nominally temperature independent.

Changing the shearing velocity (strain rate) will alter the fault-normal displacement in a velocity stepping experiment. Consider first dilation with an increase in sliding velocity. Due to anelastic effects caused by dislocation interactions (i.e., backstress), the average local strain of contacting asperities will decrease slightly, counteracting the 'direct effect' of the strain rate change. We again note that extensional plastic strains can indeed be measured during a reduction in the compressional stress (Hansen et al., 2019; 2021), particularly at small length scales (Thom et al., 2021). For a decrease in sliding velocity, fault-normal convergence leads to an increase in local asperity strain and thus an increase in the backstress resisting further deformation. The combined linearized stability term can be written as

$$a - b \approx \frac{\sqrt{3}\left(\frac{RT\sigma_{\mathrm{P}}}{E} - (\sigma_{\mathrm{b,max}} - \sigma_{\mathrm{b,0}})\gamma\beta\right)}{H}. \qquad \text{Eq. 18}$$

Thus, velocity-weakening friction can only occur when the reduction of backstress due to anelastic effects of asperities is of a larger magnitude than the increase in resistance due to the thermal rate-dependence.

Importantly, the same magnitude change in asperity strain does not always produce the same magnitude change in backstress, as it also depends on the initial backstress (i.e., the strain-hardening modulus is itself a function of strain). This is demonstrated in Figure 2, which shows the normalized backstress (the backstress divided by the maximum backstress) as a function of plastic asperity strain. The tangent of this line (the strain-hardening modulus) changes with strain. Numerous constitutive laws have been derived to describe strain hardening behavior in metals (e.g., Taylor, 1934; Mott, 1952; Armstrong & Frederick, 1966; Kocks, 1976; Sevillano et al., 1980; Estrin & Mecking, 1984; Kocks, 2001; Sinclair et al.,

2006), and it is this evolution of backstress with GND density (here, indirectly through Eq. 10) that ultimately controls 'state evolution' in our microphysical friction model.

Further refinements could be made to this theory by explicitly modeling dislocation nucleation and storage rates with dynamic and static recovery mechanisms (e.g., Breithaupt, 2021), but this is beyond the scope of the current manuscript. Furthermore, subtle variations in the fault-normal strain rate (and therefore backstress and real contact area evolution) could also be determined by explicitly writing out H as a flow law, but this is also beyond the current scope.

The same strain-hardening concept holds for a slide-hold-slide experiment. During quasi-stationary contact, the fault-normal displacement converges with time, leading to an increase in the backstress that must be overcome upon re-initiation of sliding. Importantly, as sliding continues, anelastic effects again modify the backstress as it evolves back to the steady-state value (i.e., the dislocation density evolves).

4.3 Determining the critical slip distance and the role of indentation hardness

We now derive the critical slip distance predicted by the microstructural model. Recall that the backstress acting within asperities directly corresponds to a GND density through Eq. 5 (the Taylor equation). Physically, the GND density represents curvature in the crystal lattice that has a well-defined length scale that is a radius of curvature R_c from so-called 'strain gradient plasticity,' or length-scale dependent plasticity laws (e.g., Nix & Gao, 1998), given by

$$R_c = \frac{1}{b_v \rho_{GND}}, \qquad \text{Eq. 19}$$

where b_v is the Burgers vector (lattice spacing). Because indentation hardness H is the only scale-dependent term, the length scale in Eq. 19 must arise through that term, although we have neglected the scale-dependence thus far for simplicity and clarity.

We now assume that H can be written as the sum of two terms (i.e., a scale-independent 'yield stress,' neglecting the strain-rate dependence acknowledged above, and a scale-dependent backstress due to geometry at the surface), similarly to Eq. 8 (i.e., $H = \sigma_y + \sigma_{b,H}$). Because H controls the real contact area (Eq. 11), and thus the distribution of contact area and contact patches, the backstress associated with

401 *H*, which we define as $\sigma_{b,H}$, controls the asperity size and thus the 'critical slip distance'. Interestingly, this
402 physical description predicts a gradient in backstress, or dislocation density, with the highest values nearest
403 the fault surface decaying away into the bulk rock. The curvature of the free surfaces reflect backstress very
404 near the surface (i.e., related to *H*), while the backstress in the volume of the asperity controls the overall
405 shear strength, which is able to evolve.

406 An independent estimate of surface curvature (and therefore GND density at the surface) can also
407 be obtained from topographic measurements (e.g., Jacobs et al., 2017), which are thought to reflect scale-
408 dependent strength (Brodsky et al., 2016; Thom et al., 2017). Combining Eqs. 5 and 19 and multiplying by
409 a factor of 2 to convert the radius of curvature to an asperity diameter results in a predicted length scale D_c
410 over which backstress (and thus friction) evolves:

411 $$D_c = \frac{2\alpha^2 G^2 b_v}{\sigma_{b,H}^2} \quad . \qquad \text{Eq. 20}$$

412 This value is nominally independent of temperature (except weakly through the modulus and coefficient of
413 thermal expansion), but a dependence of the backstress on temperature through the indentation hardness
414 will be discussed below.

415 We note our equation to describe fault stability (Eq. 18) inherently depends on length scale, as
416 indentation hardness is a scale-dependent property in geologic materials (e.g., Kumamoto et al., 2017;
417 Thom et al., 2017; Thom et al., 2018; Thom & Goldsby, 2019; Koizumi et al., 2020). However, we reiterate
418 that the microphysics of this model naturally gives rise to a length scale, which we present in Eq. 20. We
419 interpret this length scale as the size of a characteristic (either average or maximum) plastically deforming
420 asperity, consistent with previous interpretations of D_c. The shear strength of asperities must therefore
421 evolve over this length scale. The indentation hardness used in Eq. 18 and elsewhere in this manuscript
422 should reflect deformation at this length scale. In several of the room temperature calculations presented in
423 Section 5, we utilize the indentation hardness of olivine using the values reported in Kumamoto et al.
424 (2017). We note that because *H* and the real contact area A_r are related (Eq. 16), it is not surprising that

friction appears to evolve with changes in the real contact area. However, it is the evolution of backstress within asperities controlling their shear strength that ultimately dictates the frictional behavior.

5. Discussion

5.1 Testable predictions and future laboratory experiments

Several predictions of frictional behavior at room and elevated temperature, and the transition to bulk deformation (i.e., a 'brittle-ductile' transition) can be made using the equations derived above. Writing the full equation for the friction coefficient (just as we wrote Eq. 1 for the full RSF equation) results in a lengthy, complex equation, but nearly all values are well-constrained for olivine:

$$\mu \approx \underbrace{\frac{\sqrt{3}\left(\frac{RT\sigma_{\mathrm{P}}}{E}\sinh^{-1}\left[\frac{\dot{\varepsilon}}{A\rho}\exp\left(\frac{E}{RT}\right)\right]+\sigma_{\mathrm{b}}\right)}{H}}_{\mu_0} + \underbrace{\sqrt{3}\frac{RT\sigma_{\mathrm{P}}}{EH}\ln\left(\frac{\dot{\varepsilon}_1}{\dot{\varepsilon}_0}\right)}_{a} + \underbrace{\frac{\sqrt{3}(\sigma_{\mathrm{b,max}}-\sigma_{\mathrm{b,0}})\gamma\beta}{H}\ln\left(\frac{\dot{\varepsilon}_1}{\dot{\varepsilon}_0}\right)}_{b} \quad \text{Eq. 21}$$

In fact, the only free parameters in Eq. 21 are β (the characteristic fault-normal anelastic strain for an e-fold change in sliding strain rate), *H*, and the initial backstress $\sigma_{\mathrm{b,0}}$, which also controls ρ. Recall that the indentation hardness *H* determines the length scale over which backstress evolves (D_c, Eq. 20), and thus its value can be found at the length scale D_c observed in experiments. Interestingly, the normalized quantities of the direct and evolution effects (i.e., $\frac{a}{\mu_0}$ and $\frac{b}{\mu_0}$) are independent of the indentation hardness (*H* drops out in the ratio, as well as the factor $\sqrt{3}$), thereby reducing the number of free parameters by combining easily obtained laboratory measurements. The magnitude of the friction rise during a velocity step should provide an independent estimate of the backstress, as all other terms in the normalized *a* parameter are known. Furthermore, a suite of slide-hold-slide experiments that reveal the healing rate will also provide another independent estimate of the backstress (see below), and the family of stress relaxation curves may also constrain the backstress $\sigma_{\mathrm{b,0}}$ acting in asperities. With the backstress value in hand, the parameter β is the only free parameter that can be fit to the 'evolution effect,' and it can be calculated from the change in

fault-normal displacement (see Appendix). This value may itself be a function of other parameters, *but its physical meaning is clear: it is the change in local asperity strain (and therefore proportional to the change in dislocation density and backstress) as a function of the change in the 'state.'* Thus, all terms in this model have microphysical meaning and together give rise to rate-and-state friction-like behavior.

We can also write a state evolution law, which captures the observed slip- and/or time-dependent behavior from Eqs. 2 and 3. Neglecting the sign function for clarity, we can write how the backstress evolves with β from our Eq. 10:

$$\sigma_{\mathrm{b}}(\beta) = \dot{\varepsilon}_{\mathrm{n}}\sigma_{\mathrm{b,max}} + (\sigma_{\mathrm{b,0}} - \dot{\varepsilon}_{\mathrm{n}}\sigma_{\mathrm{b,max}})\exp(-\gamma\beta\dot{\varepsilon}_{\mathrm{n}}). \qquad \text{Eq. 22}$$

The variable $\dot{\varepsilon}_{\mathrm{n}}$ is the fault-normal strain rate, which causes the change in backstress as a function of time. If the fault-normal strain rate is determined by the sliding strain rate (e.g., if there is a constant ratio between the two when some lateral slip is occurring), then this evolution of backstress will appear to be controlled by the sliding strain rate (as in the *slip law* and in the *slowness law* at finite sliding velocity). However, at zero slip velocity, strain (and therefore backstress, dislocation density, and friction) still increases with time during stationary contact (as in the *slowness law*), explaining the time-dependent observations in slide-hold-slide experiments and the mathematical form of the *slowness law*. Thus, our state evolution law exhibits characteristics of both conventional RSF evolution laws under different assumptions and testing conditions.

A plot of the reference friction coefficient as a function of strain rate using flow law parameters for olivine from Hansen et al. (2021) is provided in Figure 3. Each different colored line is a different initial backstress (i.e., dislocation density) normalized to the maximum backstress described in Hansen et al. (2019). For plots of 0 initial backstress, we assume a background dislocation density of 10^{10} m^{-2} typical of undeformed rocks (Toriumi & Karato, 1978). These differences in backstress correspond to potential differences in the deformation history of the frictional interface. Larger initial backstresses lead to larger initial friction coefficients, as expected, and the logarithmic dependence on strain rate is presented. Interestingly, Figure 3 demonstrates quantitative agreement with the predicted 'Byerlee friction coefficient' of 0.6-0.85 when the backstress is ~50+% of the maximum backstress (Byerlee, 1978).

A further series of predictions is plotted for room temperature using the same color coding as Figure 3. Figure 4 shows the normalized rate parameter $\frac{a}{\mu_0}$ as a function of initial strain rate for a range of backstresses (i.e., dislocation densities). Note that the *a* parameter itself (Eq. 16) nominally does not depend on strain rate or backstress. However, because the reference friction coefficient is sensitive to the initial backstress and reference strain rate, the normalized value of *a* reflects the dependence on the reference friction coefficient. Figure 5 presents the normalized state parameter $\frac{b}{\mu_0}$ as a function of the parameter β for olivine. Asperity strains corresponding to typical *b* values are in the range of 100s of microstrain, corresponding to changes in asperity backstress of 10s MPa (compared to 1800 MPa maximum backstress), reflecting the fact that these are small second-order effects on the friction coefficient. All of the values presented in Figures 4 and 5 are consistent with the typical ranges of *a* and *b* measured in experiments and can be used to constrain the average backstress within asperities, as noted above. We also note that Figure 5 demonstrates the difference between steady-state values, and we do not explicitly model the time- or slip-evolution transient of the backstress here.

We present the normalized fault stability parameter $\frac{a-b}{\mu_0}$ as a function of asperity strain at a fixed reference strain rate of 0.01 s^{-1} for a range of initial backstresses in Figure 6. Note that for velocity-weakening friction to occur, the stress change from anelastic effects of asperities must be greater than the thermal rate dependence. Because the hardening modulus itself is a function of strain, different initial backstresses give different backstress changes for the same asperity strain. Larger initial backstresses result in larger values of $\frac{a-b}{\mu_0}$ (i.e., more stable sliding), as the change in backstress is smaller for the same asperity strain. *For large enough strains, velocity-weakening is always observed.*

Figure 7 illustrates the predicted value of D_c as a function of the ratio $\frac{\sigma_{b,H}^2}{G^2}$ from Eq. 20. For a shear modulus of 30 GPa, and range of backstresses 200 MPa to 2 GPa (corresponding to a dislocation density

of approximately 2 x $10^{13\text{-}15}$ m^{-2} or an average GND spacing of 50-500 nm), the predicted value of D_c is 1-100 μm, consistent with typical measurements in geologic materials. These dislocation densities are easily measurable using high-angular resolution electron backscatter diffraction (HR-EBSD) and would provide quantitative evidence of backstresses acting within asperities.

Further experimental work is needed to quantify transient plastic deformation in many important geologic materials, which would allow for more quantitative tests of this model. Alternatively, further friction tests on materials whose transient strain hardening behavior is well-understood may be another comparison. Specifically, slide-hold-slide experiments that measure the fault-normal convergence and D_c would provide valuable estimates of changes in local asperity strain and the associated transient friction rise. Predictions for slide-hold-slide tests from this model are shown in Figures 8 and 9. Figure 8 presents the peak friction coefficient as a function of local asperity strain during a hold in quasi-stationary contact for a variety of initial backstresses. Note that at sufficiently large strains, all lines asymptote to the maximum friction corresponding to the maximum backstress. In Figure 9, we present the same data, normalized to the relevant reference friction coefficient at a reference strain rate of 0.01 s^{-1}, effectively giving an estimate of the 'healing rate' for slide-hold-slide experiments. If the plastic strain rate during the hold is known or assumed, Figures 9 can be directly compared to conventional plots of peak friction as a function of log hold time. Again, this model predicts a peak friction coefficient and a decay in the healing rate at sufficiently large strains (i.e., long enough hold times).

Observations in the laboratory support the framework suggested here. For example, Ikari et al. (2016) noted that the healing rate depended on the initial friction coefficient, which may be due to the microphysics described here. In addition, Carpenter et al. (2016) noted that the 'interseismic recovery rate' depended on the loading rate in experiments on quartz-rich rocks, an observation that is also captured within the framework here. Because of the dependence on previous deformation, experiments on pre-deformed rocks may yield different friction coefficients and RSF parameters in early portions of a friction test, as strain hardening will have already occurred and set the microstructure of the frictional interface.

5.2 Implications for lithospheric strength and the brittle-ductile transition

This model suggests that transient and steady-state friction (i.e., RSF) are both controlled by dislocation glide and backstress evolution localized in asperities, which together have an inherent dependence on temperature. We demonstrate this in Figure 10 for a wide range of initial backstresses and a fixed initial strain rate of 0.01 s^{-1}. We assume that the shear strength of the asperities follows the plasticity flow law of Hansen et al. (2019; 2021) and utilize the temperature-dependent indentation hardness of olivine from Evans & Goetze (1979). Together, the thermal dependences of these two values give rise to a slightly temperature-dependent (and therefore depth-dependent) friction coefficient. In Figure 10, we also plot the quantity $\frac{a-b}{\mu_0}$, which is independent of the indentation hardness, for an arbitrary value of β = 0.0002 as a function of temperature. At relatively low temperature, velocity-weakening friction can occur. However, at higher temperatures, this model predicts that faults become inherently stable as the rate dependence outweighs the anelastic effects of asperities.

By utilizing the available high temperature indentation data for olivine (Evans & Goetze, 1979), we also predict $\sigma_{b,II}$ as a function of temperature. We assume that $\sigma_{b,II}$ is the difference between the indentation hardness and the yield stress at the appropriate temperature, from which we calculate the GND density using the Taylor equation (Eq. 5). This prediction of D_c from Eq. 20 is plotted against available data from Boettcher et al. (2007) and King & Marone (2012) in Figure 11, revealing remarkable quantitative agreement over a wide range of temperatures.

This description of the physical mechanisms that underlie friction also provides a framework to consider the strength of the entire lithosphere. In traditional descriptions of the steady-state strength of the lithosphere, 'Byerlee friction' and thermally activated creep mechanisms deeper in the Earth bound the strength (e.g., Goetze & Evans, 1979; Brace & Kohlstedt, 1980). Often, a 'semi-brittle' region is denoted where mixed brittle and viscous deformation is inferred. This portion of the lithosphere where the largest stress is supported is also thought to be dominated by 'low-temperature plasticity' in oceanic systems (Mei et al., 2010; Hansen et al., 2019; Wallis et al., 2020).

This work has demonstrated that the frictional resistance can be described by the same microphysics as low-temperature plasticity (i.e., dislocation glide and backstress evolution), suggesting a gradual transition that is controlled by the distribution of shear along discrete faults vs. shear zones around the fault. As temperature increases, the real contact area is expected to increase (Eq. 11) due to the reduction in indentation hardness (Evans & Goetze, 1979; Kranjc et al., 2016). With increasing contact area, the magnitude and heterogeneity of stress on asperities in contact will decrease, eventually favoring bulk deformation with occasional transient localized events.

This transition is denoted in Figure 12, where we plot the frictional strength of deformation localized in asperities (at a strain rate of 0.01 s^{-1}) for a range of backstresses in comparison to bulk deformation via dry dislocation creep (Hirth & Kohlstedt, 2003) at geologic strain rates (10^{-12} s^{-1}). Where our frictional resistance at an elevated strain rate coincides with bulk deformation at a geologic strain rate, a major rheological transition is expected. We infer this transition demarcates an effective 'brittle-ductile' transition, above which frictional behavior dominates, and below which bulk viscous flow occurs. Note that Figure 12 neglects the prediction of bulk low-temperature plasticity for clarity. If bulk low-temperature plasticity is expected to occur, the depth of the 'brittle-ductile' transition will also be a function of the strain history of the deeper lithosphere, as strain hardening can increase the strength of rocks deforming by low-temperature plasticity (Hansen et al., 2019; 2021). Hansen et al. (2021) argued that dislocation creep also relies on the same microphysics as low-temperature plasticity, which was also presented as a spring and dashpot model in Thom et al. (2021). How much localization occurs may be a function of the competition between different deformation mechanisms accommodated over different thicknesses of the fault zone and transient changes in the effective stress or strain rate.

We have shown in this section that under this framework, the three major rheological regimes (frictional sliding, low-temperature plasticity, and dislocation creep) throughout the oceanic lithosphere can all be described by the relative contributions of dislocation glide, backstress evolution, and recovery mechanisms. In addition, this framework suggests that the microphysics of frictional afterslip and transient post-seismic creep are the same (i.e., dislocation glide and backstress evolution, possibly with recovery

mechanisms at high temperatures), opening up new modeling opportunities and approaches for post-seismic deformation and geodetic data.

6. Conclusion

We have presented a microphysical model of rock friction based on dislocation glide and backstress evolution that explicitly incorporates the effects of strain hardening and anelasticity. This model arises naturally from the interactions among lattice dislocations and produces behavior consistent with several observations of rate- and state-friction, namely the logarithmic dependence on strain rate (sliding velocity) and memory dependence through a 'state variable.' In this formulation, the state variable has a microphysical origin. It is the average backstress acting in asperities caused by the long-range elastic interactions among geometrically necessary dislocations. A prediction of the critical slip distance D_c is presented using length-scale dependent plasticity and is a function of the dislocation density. Analytical solutions for RSF parameters are given using known steady-state and transient plasticity flow law parameters, and the temperature dependence of frictional stability is presented. Extrapolation of steady-state deformation to high temperature reveals the depth where a brittle-ductile transition occurs, and this transition is controlled by backstress evolution in asperities and the host rock. We highlight several opportunities for future experimental or numerical work that will test predictions made here about the stability and temperature-dependent frictional behavior of rocks.

Acknowledgements

C.A.T. thanks T. Breithaupt for useful discussions. Funding was provided by NSF grant EAR-1624657.

Appendix

Here we provide the full derivation and mathematical description of our model in the framework. To derive Eq. 16, we use Eq. 15 and find the change in friction between the reference strain rate ($\dot{\varepsilon}_0$) and the new strain rate ($\dot{\varepsilon}_1$) without the subsequent evolution in the backstress (i.e., at constant backstress). We write

$$\Delta\mu_{\mathrm{rate}} = \frac{\sqrt{3}\left(\frac{RT\sigma_{\mathrm{P}}}{E}\sinh^{-1}\left[\frac{\dot{\varepsilon}_1}{A\rho}\exp\left(\frac{E}{RT}\right)\right]+\sigma_{\mathrm{b},0}\right)-\sqrt{3}\left(\frac{RT\sigma_{\mathrm{P}}}{E}\sinh^{-1}\left[\frac{\dot{\varepsilon}_0}{A\rho}\exp\left(\frac{E}{RT}\right)\right]+\sigma_{\mathrm{b},0}\right)}{H}.$$

596 Eq. A1

597 Note that the backstress term drops out, and using the approximation $\sinh^{-1}(x) \approx \ln(2x)$, we derive that

$$\Delta\mu_{\mathrm{rate}} \approx \frac{\sqrt{3}\frac{RT\sigma_{\mathrm{P}}}{E}\ln\left(\frac{2\dot{\varepsilon_1}}{A\rho}\right) - \sqrt{3}\frac{RT\sigma_{\mathrm{P}}}{E}\ln\left(\frac{2\dot{\varepsilon_0}}{A\rho}\right)}{H},$$

598 Eq. A2

599 which simplifies to

$$\Delta\mu_{\mathrm{rate}} \approx \sqrt{3}\frac{RT\sigma_{\mathrm{P}}}{EH}\ln\left(\frac{\dot{\varepsilon_1}}{\dot{\varepsilon_0}}\right).$$

600 Eq. A3

601 Thus, the magnitude of the direct effect in RSF, *a*, is approximated by

$$a \approx \sqrt{3}\frac{RT\sigma_{\mathrm{P}}}{EH}.$$

602

603 To derive Eq. 17, we determine how the backstress evolves though anelastic effects after the change

604 in strain rate. We arrive at

$$\Delta\mu_{\mathrm{state}} = \frac{\sqrt{3}\left(\frac{RT\sigma_{\mathrm{P}}}{E}\sinh^{-1}\left[\frac{\dot{\varepsilon_1}}{A\rho}\exp\left(\frac{E}{RT}\right)\right] + \sigma_{\mathrm{b},1}\right) - \sqrt{3}\left(\frac{RT\sigma_{\mathrm{P}}}{E}\sinh^{-1}\left[\frac{\dot{\varepsilon_1}}{A\rho}\exp\left(\frac{E}{RT}\right)\right] + \sigma_{\mathrm{b},0}\right)}{H},$$

605

606 Eq. A4

607 where $\Delta\mu_{\mathrm{state}}$ is the change in the friction coefficient due to the 'evolution effect'. After simplifying Eq.

608 A4, we derive

$$\Delta\mu_{\mathrm{state}} = \frac{\sqrt{3}(\sigma_{\mathrm{b},1} - \sigma_{\mathrm{b},0})}{H}.$$

609 Eq. A5

610 Substituting Eq. 10 of the main text after the new steady-state has been reached into Eq. A5 for $\sigma_{\mathrm{b},1}$ gives

$$\Delta\mu_{\mathrm{state}} = \frac{\sqrt{3}(\sigma_{\mathrm{b,max}} + (\sigma_{\mathrm{b},0} - \sigma_{\mathrm{b,max}})\exp(-\gamma\varepsilon_{\mathrm{p}}) - \sigma_{\mathrm{b},0})}{H},$$

611 Eq. A6

612 which can be simplified to

$$\Delta\mu_{\mathrm{state}} = \frac{\sqrt{3}(\sigma_{\mathrm{b,max}} - \sigma_{\mathrm{b},0})[1 - \exp(-\gamma\varepsilon_{\mathrm{p}})]}{H}$$

613 Eq. A7

614 and linearized as

$$\Delta\mu_{\mathrm{state}} \approx \frac{-\sqrt{3}(\sigma_{\mathrm{b,max}} - \sigma_{\mathrm{b},0})\gamma\varepsilon_{\mathrm{p}}}{H}$$

615 Eq. A8

for small strains. ε_{p} is the change in fault-normal asperity strain caused by an e-fold change in the sliding strain rate (sliding velocity), where positive strain is defined as closure of the fault-normal gap. We can write the change in strain as

$$\varepsilon_{\mathrm{p}} = \frac{\Delta d}{L} = \frac{d_1 - d_0}{L} \quad , \qquad \text{Eq. A9}$$

where d is the fault-normal displacement and L is a length scale related to an asperity dimension (either the asperity diameter D_c or the average root-mean-squared asperity height, which can be determined through topographic measurements). The fault-closure distance is a logarithmic function of the time in contact, such that

$$d = B\ln(t), \qquad \text{Eq. A10}$$

where B is a constant. Substituting Eq. A10 into Eq. A9 and assuming that $t = \frac{1}{\dot{\varepsilon}}$ results in

$$\varepsilon_{\mathrm{p}} = -\beta \ln\left(\frac{\dot{\varepsilon}_1}{\dot{\varepsilon}_0}\right), \qquad \text{Eq. A11}$$

where β is a characteristic strain for a given change in sliding strain rate. Substituting Eq. A11 into Eq. A8 gives the change in friction due to state evolution as a function of sliding strain rate:

$$\Delta\mu_{\mathrm{state}} \approx \frac{\sqrt{3}(\sigma_{\mathrm{b,max}} - \sigma_{\mathrm{b},0})\gamma\beta}{H} \ln\left(\frac{\dot{\varepsilon}_1}{\dot{\varepsilon}_0}\right), \qquad \text{Eq. A12}$$

which results in Eq. 17 of the main text:

$$b \approx \frac{\sqrt{3}(\sigma_{\mathrm{b,max}} - \sigma_{\mathrm{b},0})\gamma\beta}{H}.$$

Tables

Table 1: List of parameters defined or used in this study.

Parameter	Symbol	Value (if used) and reference
Direct effect magnitude	*a*	
Material constant	*A*	*$10^{11.1}$ m^2s^{-1} (Hansen et al., 2021)*

Real contact area	A_r	
Taylor equation constant	α	*3 (Thom et al., 2021)*
Evolution effect magnitude	b	
Burgers vector	b_v	*0.5 nm (for olivine)*
Characteristic asperity strain	β	
Critical slip distance	D_c	
Activation energy	E	*827 kJ/mol (Hansen et al., 2021)*
Sliding strain rate	$\dot{\varepsilon}$	
Fault-normal strain rate	$\dot{\varepsilon_n}$	
Plastic strain rate	$\dot{\varepsilon_p}$	
Low-T plasticity strain rate	$\dot{\varepsilon}_{LTP}$	
Asperity strain	ε_p	
Normal force	F_n	
Friction force	F_f	
Shear modulus	G	*75 GPa (for olivine)*
Material constant	γ	*75 (Hansen et al., 2019)*
Indentation hardness	H	*10 GPa (room temperature, Kumamoto et al., 2017); variable (elevated temperature, Evans & Goetze, 1979)*
Friction coefficient	μ	
Stress exponent	n	
Low-temperature plasticity flow law constant	p	
Pressure	P	
Low-temperature plasticity flow law constant	q	
Gas constant	R	*8.314 J K^{-1} mol^{-1}*
Radius of curvature	R_c	
Dislocation density	ρ	

Geometrically necessary dislocation density	ρ_{GND}	
Differential stress	σ	
Backstress	σ_b	
Indentation backstress	$\sigma_{b,H}$	
Maximum backstress	$\sigma_{b,max}$	*1.8 GPa (Hansen et al., 2019)*
Peierls stress	σ_p	*3.1 GPa (Hansen et al., 2019)*
Yield stress	σ_y	
Time	t	
Absolute temperature	T	
Asperity shear strength	τ	
State variable	θ	
Sliding velocity	V	
Activation volume	V^*	
Asperity thickness	X	

Figures

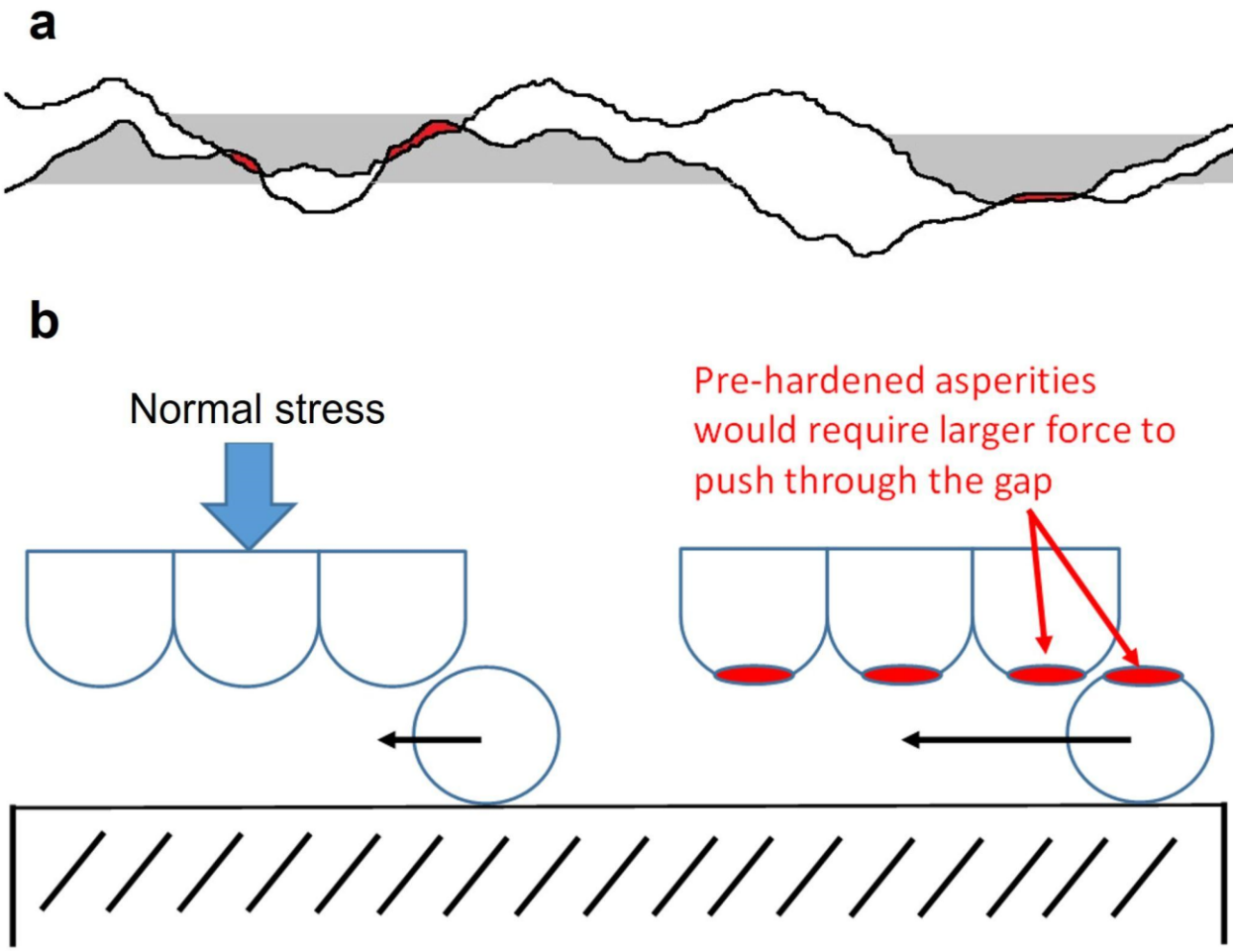

Figure 1: In (a), a schematic of two rough surfaces coming into static contact. Note that where overlap occurs between the surfaces (shown in red), plastic deformation governed by the indentation hardness is expected to occur due to the large contact stresses. This deformation determines the real contact area, while the region of an asperity that must deform to allow frictional sliding is shaded schematically in gray. In (b), we schematically demonstrate asperities sliding past one another. The hatched region represents a rigid, frictionless plane that the circles move across. A periodic array of asperities are shown with an applied normal stress. In order to slide the circular asperity through the gap, some deformation must occur at the tips of the asperities, whether it be elastic or plastic. On the left in (b), we show with the black arrow how much force is required for sliding. On the right in (b), we highlight in red areas that are pre-deformed (i.e., the asperities have a strain-hardening history), which increases the frictional resistance opposing

motion of the asperity through the gap. Thus, by increasing the local strength of asperities through pre-hardening, the friction force is increased for the schematic on the right in (b).

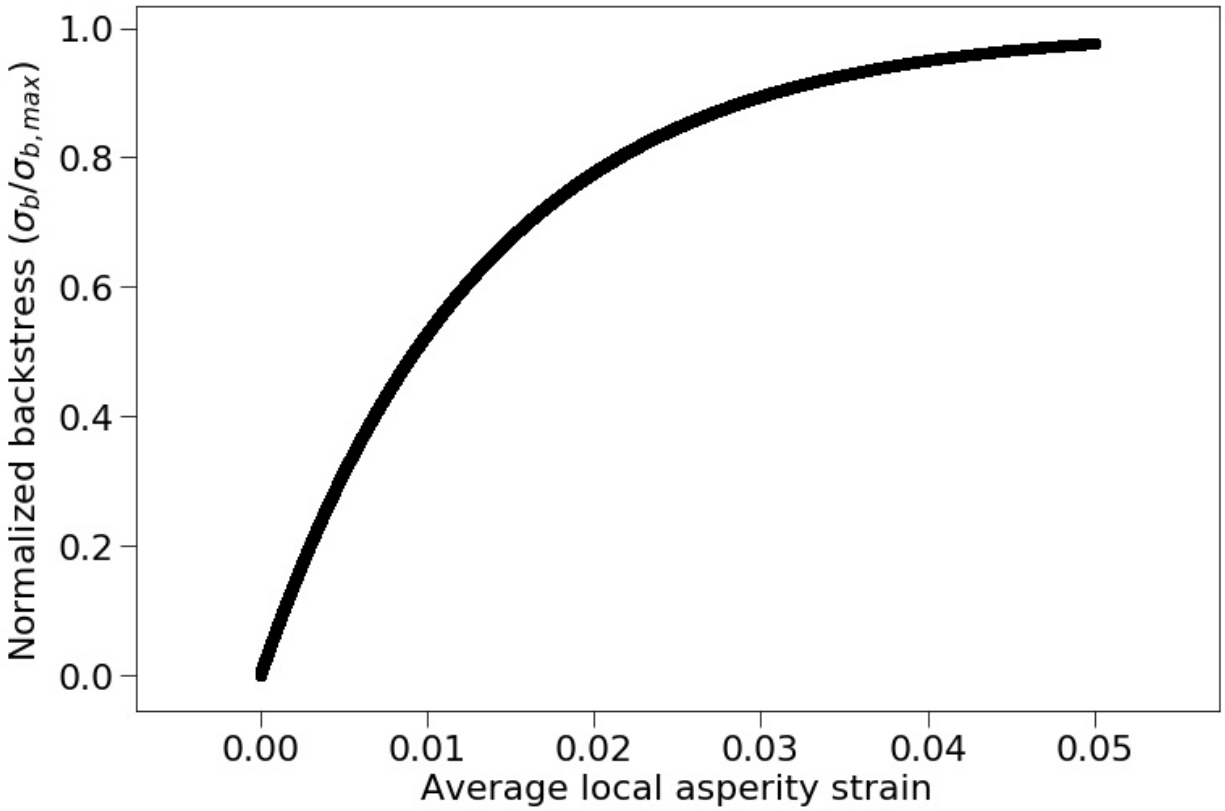

Figure 2: Normalized backstress as a function of average local asperity strain for $\gamma = 75$. Recall that 'strain' is physically a proxy for backstress or geometrically necessary dislocation density in the contacting asperities.

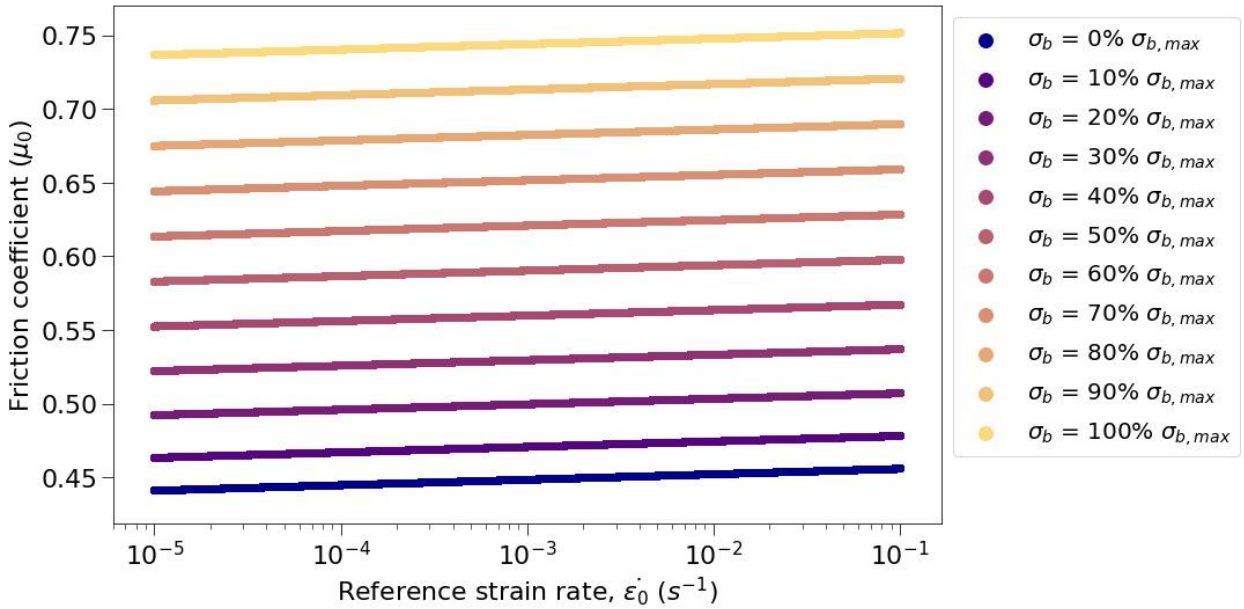

Figure 3: Friction coefficient μ_0 as a function of reference strain rate for olivine at room temperature. Each line represents a given initial backstress, which is shown relative to the maximum backstress in the legend. We assume H = 10 GPa here, a value consistent with results from Kumamoto et al., (2017). All other flow law parameters are taken from Hansen et al. (2021). For σ_b = 0, we assume a background dislocation density of 10^{10} m^{-2} after Toriumi & Karato, (1978).

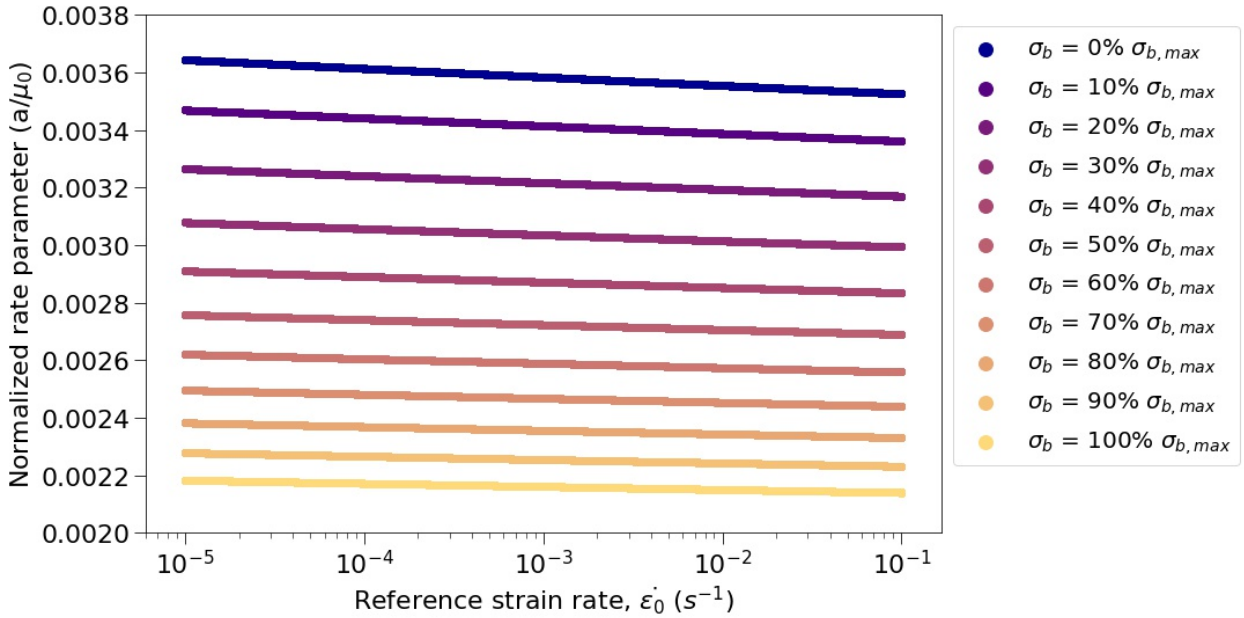

Figure 4: The normalized rate parameter as a function of reference strain rate for several different values of the initial backstress. Larger values of backstress lead to a smaller rate dependence because a larger proportion of the stress on asperities is supported by long-range elastic interactions among dislocations. The quantity $\frac{a}{\mu_0}$ is independent of the indentation hardness and can be used to constrain the initial backstress at reference friction coefficient μ_0.

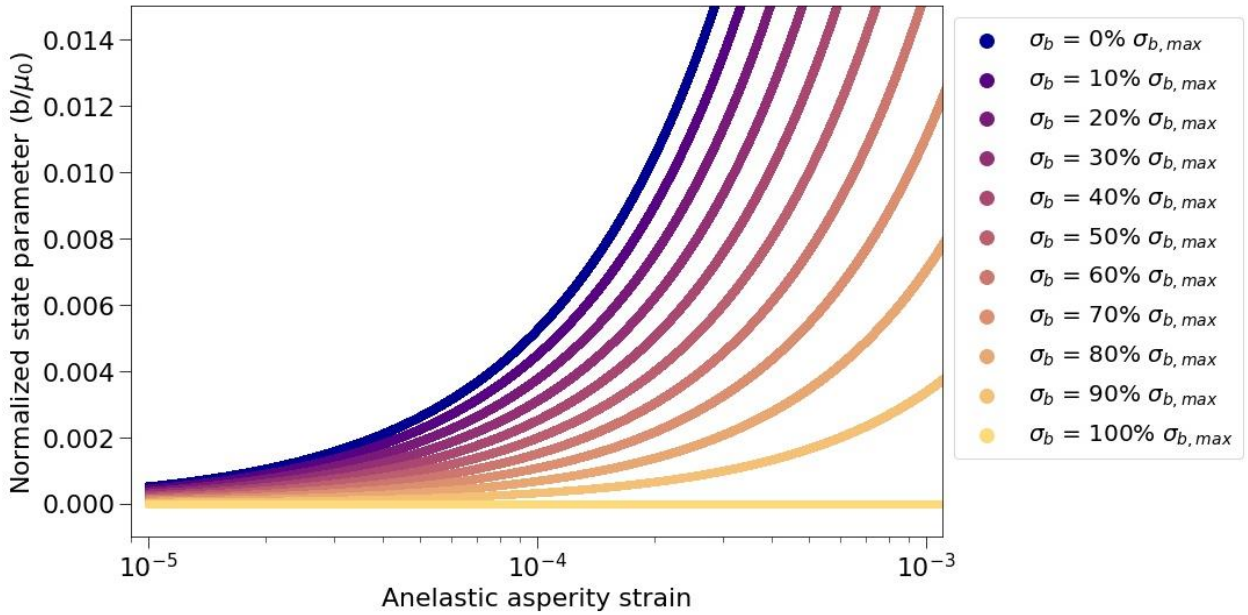

Figure 5: The normalized state parameter $\frac{b}{\mu_0}$ as a function of asperity strain resulting from an e-fold change in strain rate (i.e., different values of β). This value is independent of the indentation hardness. However, with a known initial backstress and indentation hardness, the only free parameter in our model is the anelastic asperity strain, which gives rise to a change in backstress. This asperity strain is expected to evolve over the length scale described in Eq. 20.

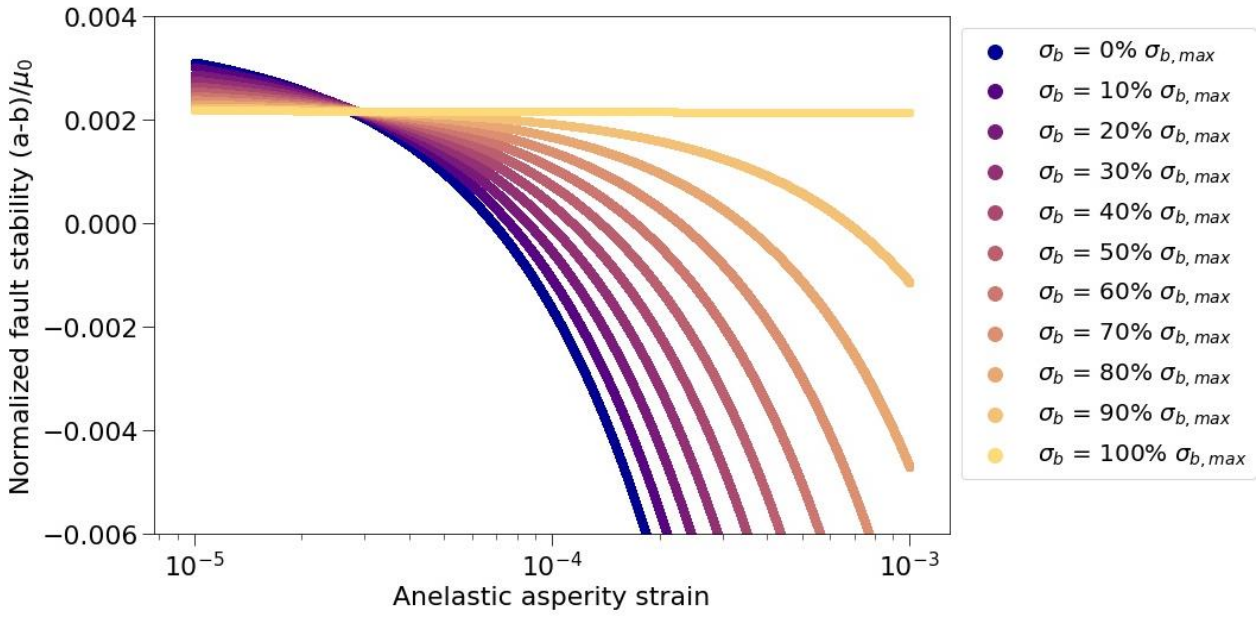

672

673 *Figure 6: A normalized approximation of fault stability (the quantity* $\frac{a-b}{\mu_0}$ *) as a function of anelastic*
674 *asperity strain at a reference strain rate of 0.01* s^{-1} *at room temperature for a range of initial backstresses.*
675 *Note that velocity-weakening friction can only occur when the stress reduction from anelastic effects*
676 *outweighs the increase in stress from the strain rate dependence. Importantly, because the hardening*
677 *modulus is a function of strain, the same asperity strain does not produce the same change in backstress.*

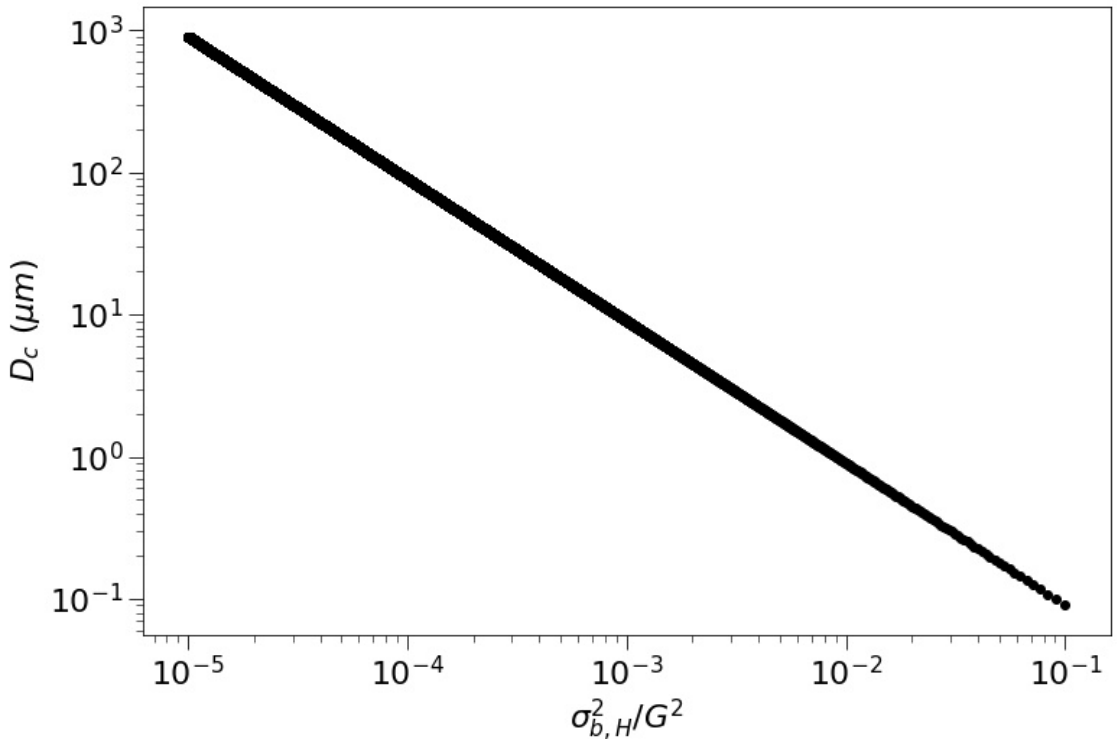

Figure 7: The predicted value of D_c as a function of the ratio $\frac{\sigma^2_{\mathrm{b,H}}}{G^2}$, based on Eq. 20. For a fixed shear modulus, D_c increases with decreasing backstress. This is because a smaller GND density allows for a larger radius of curvature at the free surface, or asperity size.

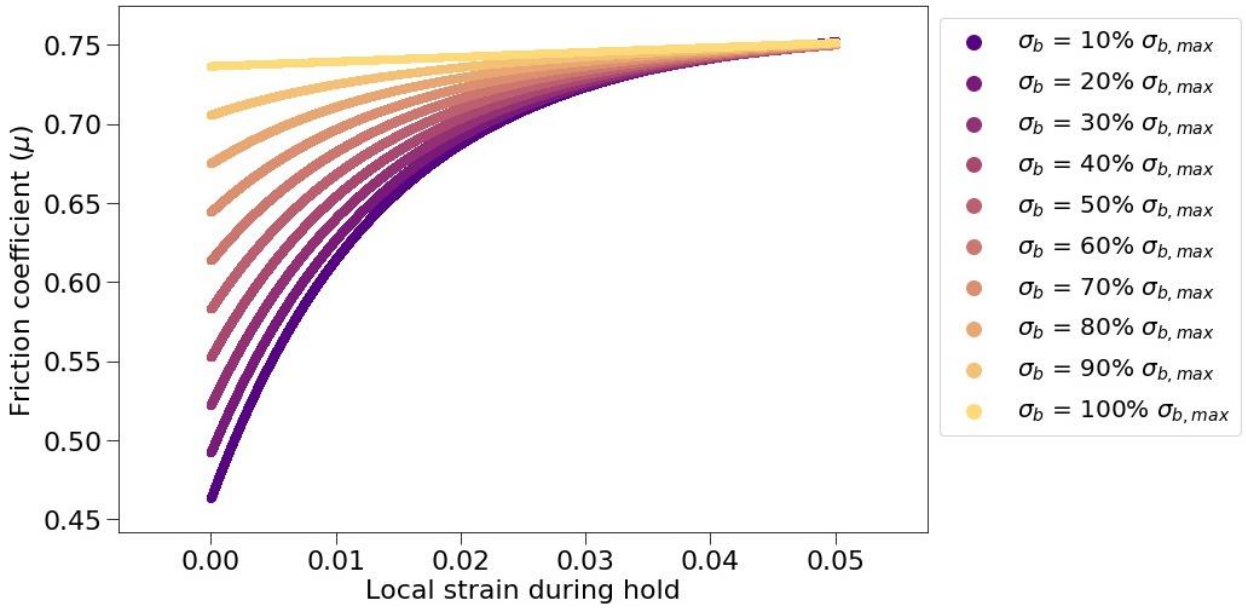

Figure 8: A prediction of the peak friction coefficient using olivine flow law parameters as a function of local asperity strain change during a hold in quasi-stationary contact. Note that the rise in friction with increasing local strain is a function of the initial backstress, and all lines asymptote to a maximum friction coefficient, corresponding to a maximum backstress.

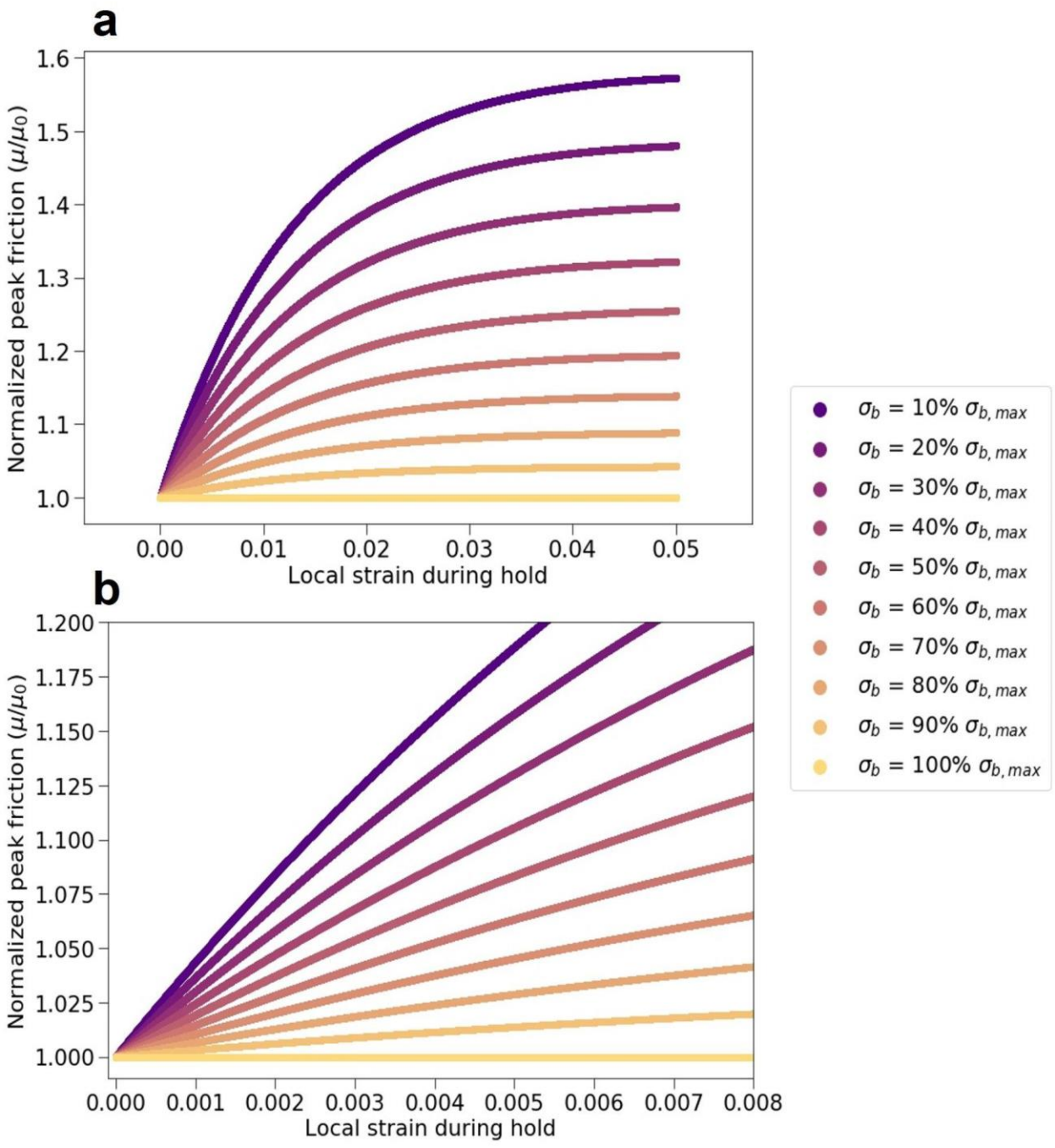

Figure 9: The same data as in Figure 8, normalized to the reference friction coefficient at a given backstress value assuming a reference strain rate of 0.01 s^{-1}. Again, note in (a) that the friction rise is predicted to saturate at sufficiently large strain (alternatively, sufficiently long time), and the 'healing rate' measured in slide-hold-slide experiments depends on the initial backstress. In (b), we highlight the approximately linear dependence of peak friction on strain for small strains.

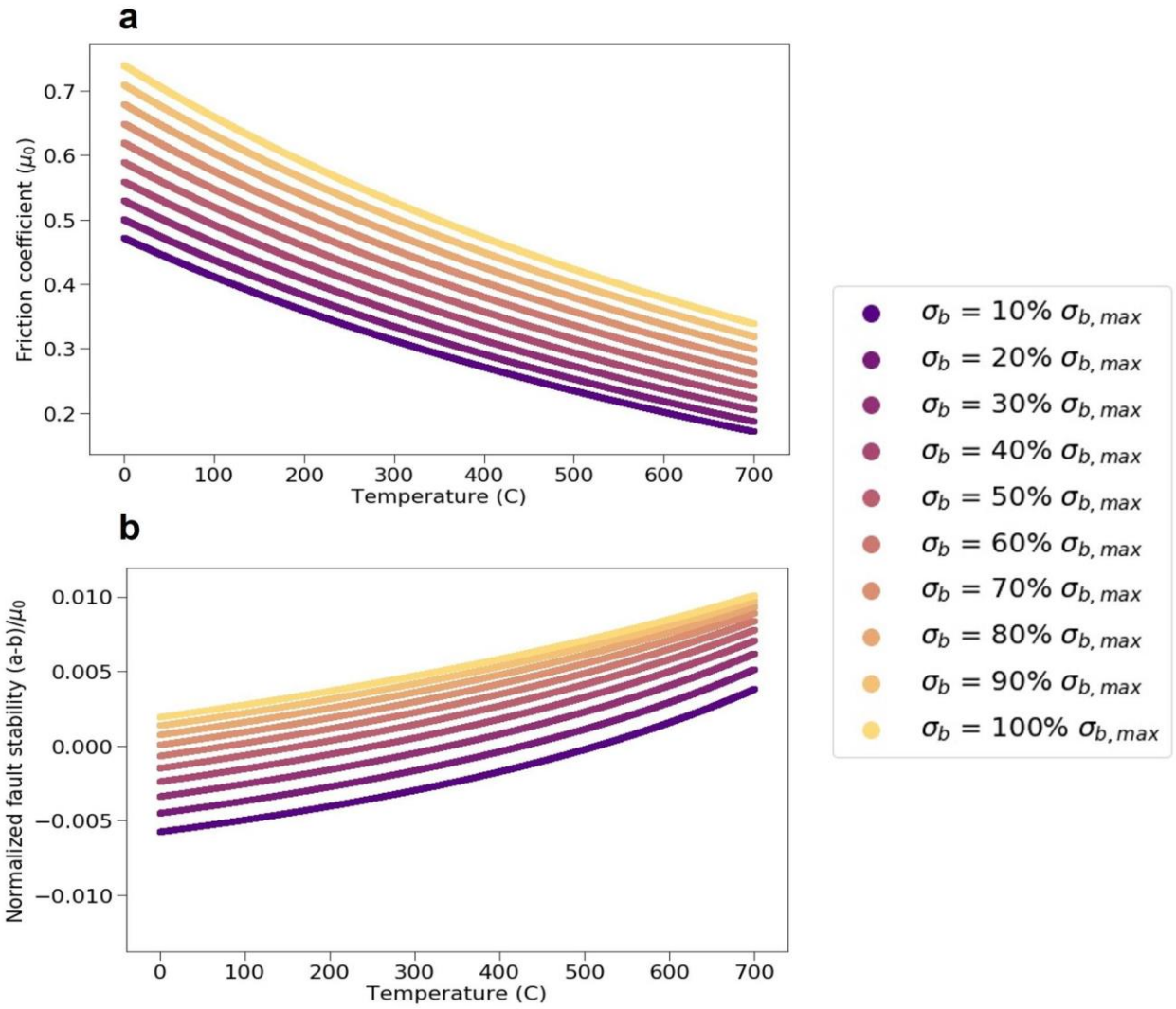

Figure 10: In (a), the predicted value of the reference friction coefficient as a function of temperature at a fixed reference strain rate of 0.01 s^{-1}. At high temperature, the friction coefficient appears to increase due to the indentation hardness decreasing faster than the shear strength of asperities. In (b), the value $\frac{a-b}{\mu_0}$ is plotted for a fixed change in asperity strain of 0.0002 for a range of initial backstresses. Note that this quantity is independent of the indentation hardness and fault stability increases with temperature. Larger initial backstresses lead to inherently more stable sliding than smaller backstresses.

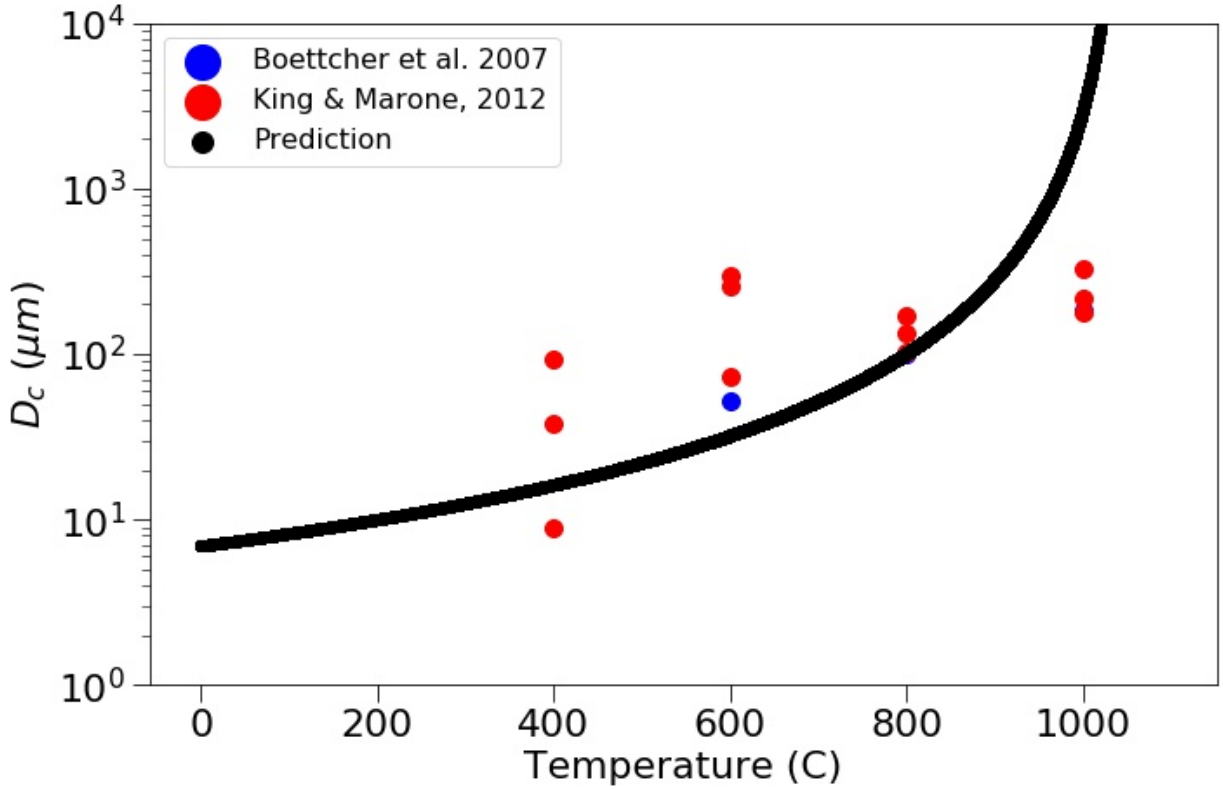

Figure 11: A comparison of the predicted value of D_c as a function of temperature to published data in Boettcher et al., (2007) and King & Marone (2012). To determine the backstress, we assume that indentation hardness can be written as the sum of a yield stress term and a backstress term. We use the hot indentation hardness data of Evans & Goetze (1979) to determine the value $\sigma_{b,II}$, assuming the thermal activation parameters for the yield stress from Hansen et al. (2021). These backstress values are converted to predicted D_c values using Eqs. 5, 19, and 20.

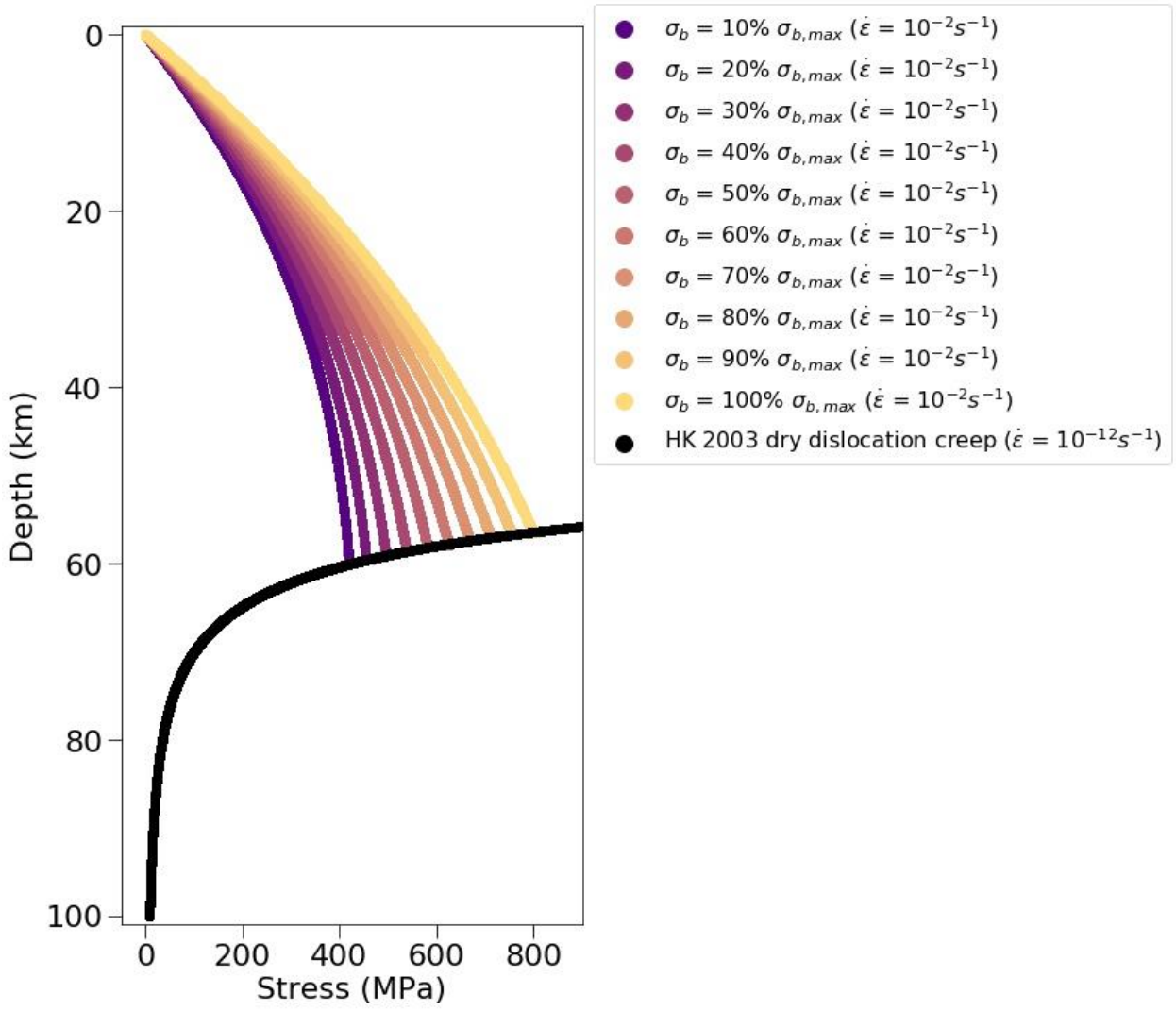

Figure 12: Predicted strength of oceanic lithosphere, approximated by olivine deforming by bulk dislocation creep and localized plasticity in asperities (frictional sliding). Each colored line represents the resistance of asperities at a given backstress shown in the legend, assuming a linear overburden normal stress of 27 MPa/km, an asperity strain rate of 10^{-2} s^{-1}, and the indentation hardness data of Evans & Goetze, (1979). The geothermal gradient is determined assuming a mantle potential temperature of 1300°C and 80-Myr-old crust after Turcotte & Schubert, (2014). The black line is the prediction of the Hirth & Kohlstedt (2003) dry dislocation creep flow law at a strain rate of 10^{-12} s^{-1}. The point of intersection between the frictional sliding lines and bulk deformation represents the point at which it is equally difficult to deform the bulk rock as to slide on locally deforming asperities, which we take to represent a rheological transition

from frictional to bulk viscous flow (i.e., a 'brittle-ductile' transition). This transition is predicted to occur at approximately 60 km depth in this figure, but changes in the strain rate or mineralogy may alter the depth of this transition.

References

1. Aharonov, E., & Scholz, C.H. (2018). A physics-based rock friction constitutive law: Steady state friction. *Journal of Geophysical Research: Solid Earth*, *123*(2), 1591-1614. https://doi.org/10.1002/2016JB013829
2. Aharonov, E., & Scholz, C.H. (2019). The brittle-ductile transition predicted by a physics-based friction law. *Journal of Geophysical Research: Solid Earth*, *124*(3), 2721-2737. https://doi.org/10.1029/2018JB016878
3. Ampuero, J.-P., & Rubin, A.M. (2008). Earthquake nucleation on rate and state faults - Aging and slip laws. *Journal of Geophysical Research: Solid Earth*, *113*(B1), https://doi.org/10.1029/2007JB005082
4. Armstrong, P.J., & Frederick, C.O. (1966). *A Mathematical Representation of the Multiaxial Bauschinger Effect*. Berkeley Nuclear Laboratory.
5. Ashby, M.F. (1970). The deformation of plastically non-homogeneous materials. *The Philosophical Magazine: A Journal of Theoretical Experimental and Applied Physics*, *8*(21), 399-424. https://doi.org/10.1080/14786437008238426
6. Barbot, S. (2019). Modulation of fault strength during the seismic cycle by grain-size evolution around contact junctions. *Tectonophysics*, *765*, 129-145. https://doi.org/10.1016/j.tecto.2019.05.004
7. Bar-Sinai, Y., Spatschek, R., Brener, E.A., & Bouchbinder, E. (2014). On the velocity-strengthening behavior of dry friction. *Journal of Geophysical Research: Solid Earth*, *119*(3), 1738-1748. https://doi.org/10.1002/2013JB010586

8. Bhattacharya, P., Rubin, A.M., Bayart, E., Savage, H.M., & Marone, C. (2015). Critical evaluation of state evolution laws in rate and state friction: Fitting large velocity steps in simulated fault gouge with time-, slip-, and stress-dependent constitutive laws. *Journal of Geophysical Research: Solid Earth*, *120*(9), 6365-6385. https://doi.org/10.1002/2015JB012437
9. Bhattacharya, P., Rubin, A.M., & Beeler, N.M. (2017). Does fault strengthening in laboratory rock friction experiments really depend primarily upon time and not slip? *Journal of Geophysical Research: Solid Earth*, *122*(8), 6389-6430. https://doi.org/10.1002/2017JB013936
10. Blanpied, M.L., Lockner, D.A., & Byerlee, J.D. (1991). Fault stability inferred from granite sliding experiments at hydrothermal conditions. *Geophysical Research Letters*, *18*(4), 609-612. https://doi.org/10.1029/91GL00469
11. Blanpied, M.L., Lockner, D.A., & Byerlee, J.D. (1995). Frictional slip of granite at hydrothermal conditions. *Journal of Geophysical Research: Solid Earth*, *100*(B7), 13045-13064. https://doi.org/10.1029/95JB00862
12. Blanpied, M.L., Marone, C.J., Lockner, D.A., Byerlee, J.D., & King, D.P. (1998). Quantitative measure of the variation in fault rheology due to fluid-rock interactions. *Journal of Geophysical Research: Solid Earth*, *103*(B5), 9691-9712. https://doi.org/10.1029/98JB00162
13. Boettcher, M.S., Hirth, G., & Evans, B. (2007). Olivine friction at the base of oceanic seismogenic zones. *Journal of Geophysical Research: Solid Earth*, *112*(B1), https://doi.org/10.1029/2006JB004301
14. Bos, B., & Spiers, C.J. (2002). Fluid-assisted healing processes in gouge-bearing faults: Insights from experiments on a rock analogue system. *Pure and Applied Geophysics*, *159*, 2537-2566. https://doi.org/10.1007/s00024-002-8747-2
15. Bowden, F.P., & Tabor, D. (1950). *The Friction and Lubrication of Solids.* Clarendon Press.
16. Brace, W.F., & Kohlstedt, D.L. (1980). Limits on lithospheric stress imposed by laboratory experiments. *Journal of Geophysical Research: Solid Earth*, *85*(B11), 6248-6252. https://doi.org/10.1029/JB085iB11p06248

17. Brechet, Y., & Estrin, Y. (1994). The effect of strain rate sensitivity on dynamic friction of metals. *Scripta Metallurgica et Materialia*, *30*(11), 1449-1454. https://doi.org/10.1016/0956-716x(94)90244-5
18. Breithaupt, T. (2021). Modelling elements of microstructure in olivine. D.Phil. thesis, University of Oxford.
19. Brodsky, E.E., Kirkpatrick, J.D., & Candela, T. (2016). Constraints from fault roughness on the scale-dependent strength of rocks. *Geology*, *44*(1), 19-22. https://doi.org/10.1130/G37206.1
20. Bush, A.W., Gibson, R.D., & Thomas, T.R. (1975). The elastic contact of a rough surface. *Wear*, *35*(1), 87-111. https://doi.org/10.1016/0043-1648(75)90145-3
21. Byerlee, J. (1978). Friction of rocks. *Pure and Applied Geophysics*, *116*, 615-626. https://doi.org/10.1007/BF00876528
22. Candela, T., Renard, F., Klinger, Y., Mair, K., Schmittbuhl, J., & Brodsky, E.E. (2012). Roughness of fault surfaces over nine decades of length scales. *Journal of Geophysical Research: Solid Earth*, *117*(B8), https://doi.org./10.1029/2011JB009041
23. Carpenter, B.M., Ikari, M.J., & Marone, C. (2016). Laboratory observations of time-dependent frictional strengthening and stress relaxation in natural and synthetic fault gouges. *Journal of Geophysical Research: Solid Earth*, *121*(2), 1183-1201. https://doi.org/10.1002/2015JB012136
24. Chen, J., Niemeijer, A.R., & Spiers, C.J. (2017). Microphysically derived expressions for rate-and-state friction parameters, a, b, and Dc. *Journal of Geophysical Research: Solid Earth*, *122*(12), 9267-9657. https://doi.org/10.1002/2017JB014226
25. Chen, J., Verberne, B.A., & Niemeijer, A.R. (2020). Flow-to-friction transition in simulated calcite gouge: Experiments and microphysical modeling. *Journal of Geophysical Research: Solid Earth*, *125*(11), e2020JB019970. https://doi.org/10.1029/2020JB019970
26. Chester, F.M. (1994). Effects of temperature on friction: Constitutive equations and experiments with quartz gouge. *Journal of Geophysical Research: Solid Earth*, *99*(B4), 7247-7261. https://doi.org/10.1029/93JB03110

27. Chester, F.M., & Higgs, N.G. (1992). Multimechanism friction constitutive model for ultrafine quartz gouge at hypocentral conditions. *Journal of Geophysical Research: Solid Earth*, *97*(B2), 1859-1870. https://doi.org/10.1029/91JB02349
28. Dieter, G.E. (1986). *Mechanical Metallurgy*. New York, NY: McGraw-Hill Education.
29. Dieterich, J.H. (1972). Time-dependent friction in rocks. *Journal of Geophysical Research*, *77*(20), 3690-3697. https://doi.org/10.1029/JB077i020p03690
30. Dieterich, J.H. (1978). Time-dependent friction and the mechanics of stick-slip. *Pure and Applied Geophysics*, *116*, 790-806. https://doi.org/10.1007/BF00876539
31. Dieterich, J.H. (1992). Earthquake nucleation on faults with rate- and state-dependent strength. *Tectonophysics*, *211*(1-4), 115-134. https://doi.org/10.1016/0040-1951(92)90055-B
32. Dieterich, J.H., & Kilgore, B.D. (1994). Direct observation of frictional contacts: New insights for state-dependent properties. *Pure and Applied Geophysics*, *143*, 283-302. https://doi.org/10.1007/BF00874332
33. Dieterich, J.H., & Kilgore, B.D. (1996). Imaging surface contacts: Power law contact distributions and contact stresses in quartz, calcite, glass and acrylic plastic. *Tectonophysics*, *256*(1-4), 219-239. https://doi.org/10.1016/0040-1951(95)00165-4
34. Estrin, Y., & Brechet, Y. (1996). On a model of frictional sliding. *Pure and Applied Geophysics*, *147*, 745-762. https://doi.org/10.1007/BF01089700
35. Estrin, Y., & Mecking, H. (1984). A unified phenomenological description of work hardening and creep based on one-parameter models. *Acta Metallurgica*, *32*(1), 57-70. https://doi.org/10.1016/0001-6160(84)90202-5
36. Evans, B., & Goetze, C. (1979). The temperature variation of hardness of olivine and its implication for polycrystalline yield stress. *Journal of Geophysical Research: Solid Earth*, *84*(B10), 5505-5524. https://doi.org/10.1029/JB084iB10p05505
37. Frost, H.J., & Ashby, M.F. (1982). *Deformation-mechanism maps: The plasticity and creep of metals and ceramics*. Oxford University Press.

38. Goetze, C., & Evans, B. (1979). Stress and temperature in the bending lithosphere as constrained by experimental rock mechanics. *Geophysical Journal International*, *59*(3), 465-478. https://doi.org/10.1111/j.1365-246X.1979.tb02567.x

39. Greenwood, J.A., & Williamson, J.B.P. (1966). Contact of nominally flat surfaces. *Proceedings of the Royal Society of London A*, *295*, 300-319. https://doi.org/10.1098/rspa.1966.0242

40. Gu, J.-C., Rice, J.R., Ruina, A.L., & Tse, T.S. (1984). Slip motion and stability of a single degree of freedom elastic system with rate and state dependent friction. *Journal of the Mechanics and Physics of Solids*, *32*(3), 167-196. https://doi.org/10.1016/0022-5096(84)90007-3

41. Hansen, L.N., Kumamoto, K.M., Thom, C.A., Wallis, D., Durham, W.B., Goldsby, D.L., et al. (2019). Low-temperature plasticity in olivine: Grain size, strain hardening, and the strength of the lithosphere. *Journal of Geophysical Research*, *124*(6), 5427-5449. https://doi.org/10.1029/2018JB016736

42. Hansen, L.N., Wallis, D., Breithaupt, T., Thom, C.A., & Kempton, I. (2021). Dislocation creep of olivine: Backstress evolution controls transient creep at high temperatures. *Journal of Geophysical Research: Solid Earth*, *126*(5), e2020JB021325. https://doi.org/10.1029/2020JB021325

43. Harbord, C.W.A., Nielsen, S.B., De Paola, N., & Holdsworth, R.E. (2018). Earthquake nucleation on rough faults. *Geology*, *45*(10), 931-934. https://doi.org/10.1130/G39181.1

44. Hatano, T. (2015). Rate and state friction law as derived from atomistic processes at asperities. *ArXiv*, https://arxiv.org/abs/1512.05078

45. Hawthorne, J.C., & Rubin, A.M. (2013a). Tidal modulation and back-propagating fronts in slow slip events simulated with a velocity-weakening to velocity-strengthening friction law. *Journal of Geophysical Research: Solid Earth*, *118*(3), 1216-1239. https://doi.org/10.1002/jgrb.50107

46. Hawthorne, J.C., & Rubin, A.M. (2013b). Laterally propagating slow slip events in a rate and state friction model with a velocity-weakening to velocity-strengthening transition. *Journal of Geophysical Research: Solid Earth*, *118*(7), 3785-3808. https://doi.org/10.1002/jgrb.50261

47. Hirth, G., & Kohlstedt, D. (2003). Rheology of the upper mantle and the mantle wedge: A view from the experimentalists. *Geophysical Monograph - American Geophysical Union*, *138*, 83-106. https://doi.org/10.1029/138gm06

48. Hyun, S., Pei, L., Molinari, J.-F., & Robbins, M.O. (2004). Finite-element analysis of contact between self-affine surfaces. *Physical Review E*, *70*, 026117. https://doi.org/10.1103/PhysRevE.70.026117

49. Ikari, M.J., Marone, C., Saffer, D.M., & Kopf, A.J. (2013). Slip weakening as a mechanism for slow earthquakes. *Nature Geoscience*, *6*, 468-472. https://doi.org/10.1038/ngeo1818

50. Ikari, M.J., Carpenter, B.M., & Marone, C. (2016). A microphysical interpretation of rate- and state-dependent friction for fault gouge. *Geochemistry, Geophysics, Geosystems*, *17*(5), 1660-1677. https://doi.org/10.1002/2016GC006286

51. Im, K., Saffer, D., Marone, C., & Avouac, J.-P. (2020). Slip-rate-dependent friction as a universal mechanism for slow slip events. *Nature Geoscience*, *13*, 705-710. https://doi.org/10.1038/s41561-020-0627-9

52. Jacobs, T.D.B., Junge, T., & Pastewka, L. (2017). Quantitative characterization of surface topography using spectral analysis. *Surface Topography: Metrology and Properties*, *5*, 013001. https://doi.org/10.1088/2051-672X/aa51f8

53. Jain, C., Korenaga, J., & Karato, S.-I. (2017). On the yield strength of oceanic lithosphere. *Geophysical Research Letters*, *44*(19), 9716-9722. https://doi.org/10.1002/2017GL075043

54. Kaproth, B.M., & Marone, C. (2013). Slow earthquakes, preseismic velocity changes, and the origin of slow frictional stick-slip. *Science*, *341*(6151), 1229-1232. https://doi.org/10.1126/science.1239577

55. Kato, N., & Tullis, T.E. (2001). A composite rate- and state-dependent law for rock friction. *Geophysical Research Letters*, *28*(6), 1103-1106. https://doi.org/10.1029/2000GL012060

56. Kawazoe, T., Karato, S.-I., Otuska, K., Jing, Z., & Mookherjee, M. (2009). Shear deformation of dry polycrystalline olivine under deep upper mantle conditions using a rotational Drickamer

apparatus (RDA). *Physics of Earth and Planetary Interiors*, *174*(1-4), 128-137. https://doi.org/10.1016/j.pepi.2008.06.027

57. Kilgore, B., Lozos, J., Beeler, N.M., & Oglesby, D. (2012). Laboratory observations of fault strength in response to changes in normal stress. *Journal of Applied Mechanics*, *79*(3), 031007. https://doi.org/10.1115/1.4005883
58. Kilgore, B., Beeler, N.M., Lozos, J., & Oglesby, D. (2017). Rock friction under variable normal stress. *Journal of Geophysical Research: Solid Earth*, *122*(9), 7042-7075. https://doi.org/10.1002/2017JB014049
59. King, D.S.H., & Marone, C. (2012). Frictional properties of olivine at high temperature with applications to the strength and dynamics of the oceanic lithosphere. *Journal of Geophysical Research: Solid Earth*, *117*(B12), https://doi.org/10.1029/2012JB009511
60. Kocks, U.F. (1976). Laws for work-hardening and low-temperature creep. *Journal of Engineering Materials and Technology*, *98*(1), 76-85. https://doi.org/10.1115/1.3443340
61. Kocks, U.F. (2001). Realistic constitutive relations for metal plasticity. *Materials Science and Engineering: A*, *317*(1-2), 181-187. https://doi.org/10.1016/S0921-5093(01)01174-1
62. Koizumi, S., Hiraga, T., & Suzuki, T.S. (2020). Vickers indentation tests on olivine: Size effects. *Physics and Chemistry of Minerals*, *47*(8), https://doi.org/10.1007/s00269-019-01075-5
63. Kranjc, K., Rouse, Z., Flores, K.M., & Skemer, P. (2016). Low-temperature plastic rheology of olivine determined by nanoindentation. *Geophysical Research Letters*, *43*(1), 176-184. https://doi.org/10.1002/2015GL065837
64. Kumamoto, K.M., Thom, C.A., Wallis, D., Hansen, L.N., Armstrong, D.E.J., Warren, J.M., et al. (2017). Size effects resolve discrepancies in 40 years of work on low-temperature plasticity in olivine. *Science Advances*, *3*(9), e1701338. https://doi.org/10.1126/sciadv.1701338
65. Lapusta, N., Rice, J.R., Ben-Zion, Y., & Zheng, G. (2000). Elastodynamic analysis for slow tectonic loading with spontaneous rupture episodes on faults with rate- and state-dependent friction.

Journal of Geophysical Research: Solid Earth, *105*(B10), 23765-23789. https://doi.org/10.1029/2000JB900250

66. Leeman, J.R., Saffer, D.M., Scuderi, M.M., & Marone, C. (2016). Laboratory observations of slow earthquakes and the spectrum of tectonic fault slip modes. *Nature Communications*, *7*, 11104. https://doi.org/10.1038/ncomms11104
67. Liu, X.-Z., Ye, Z., Dong, Y., Egberts, P., Carpick, R.W., & Martini, A. (2015). Dynamics of atomic stick-slip friction examined with atomic force microscopy and atomistic simulations at overlapping speeds. *Physical Review Letters*, *114*, 146102. https://doi.org/10.1103/PhysRevLett.114.146102
68. Marone, C. (1998). Laboratory-derived friction laws and their application to seismic faulting. *Annual Review of Earth and Planetary Sciences*, *26*, 643-696. https://doi.org/10.1146/annurev.earth.26.1.643
69. Mecking, H., & Kocks, U.F. (1981). Kinetics of flow and strain-hardening. *Acta Metallurgica*, *29*(11), 1865-1975. https://doi.org/10.1016/0001-6160(81)90112-7
70. Mei, S., Suzuki, A.M., Kolstedt, D.L., Dixon, N.A., & Durham, W.B. (2010). Experimental constraints on the strength of the lithospheric mantle. *Journal of Geophysical Research: Solid Earth*, *115*(B8), https://doi.org/10.1029/2009JB006873
71. Molinari, A., & Perfettini, H. (2017). A micromechanical model of rate and state friction: 2. Effect of shear and normal stress changes. *Journal of Geophysical Research: Solid Earth*, *122*(4), 2638-2652. https://doi.org/10.1002/2016JB013307
72. Mott, N.F. (1952). The mechanism of work-hardening of metals. *Proceedings of the Institution of Mechanical Engineers*, *166*(1), https://doi.org/10.1243/PIME_PROC_1952_166_042_02
73. Nagata, K., Nakatain, M., & Yoshida, S. (2008). Monitoring frictional strength with acoustic wave transmission. *Geophysical Research Letters*, *35*(6), https://doi.org/10.1029/2007GL033146
74. Nagata, K., Nakatani, M., & Yoshida, S. (2012). A revised rate- and state-dependent friction law obtained by constraining constitutive and evolution laws separately with laboratory data. *Journal of Geophysical Research: Solid Earth*, *117*(B2), https://doi.org/10.1029/2011JB008818

75. Nagata, K., Kilgore, B., Beeler, N.M., & Nakatani, M. (2014). High-frequency imaging of elastic contrast and contact area with implications for naturally observed changes in fault properties. *Journal of Geophysical Research: Solid Earth*, *119*(7), 5855-5875. https://doi.org/10.1002/2014JB011014

76. Nakatani, M. (2001). Conceptual and physical clarification of rate and state friction: Frictional sliding as a thermally activated rheology. *Journal of Geophysical Research: Solid Earth*, *106*(B11), https://doi.org/10.1029/2000JB900453

77. Niemeijer, A.R., & Spiers, C.J. (2007). A microphysical model for strong velocity weakening in phyllosilicate-bearing fault gouges. *Journal of Geophysical Research: Solid Earth*, *112*(B10), https://doi.org/10.1029/2007JB005008

78. Nix, W.D., & Gao, H. (1998). Indentation size effects in crystalline materials: A law for strain gradient plasticity. *Journal of the Mechanics and Physics of Solids*, *46*(3), 411-425. https://doi.org/10.1016/S0022-5096(97)00086-0

79. Noda, H., & Takahashi, M. (2016). The effective stress law at a brittle-plastic transition with a halite gouge layer. *Geophysical Research Letters*, *43*(5), 1966-1972. https://doi.org/10.1002/2015GL067544

80. Okamoto, K.K., Brodsky, E.E., Thom, C.A., Smeraglia, L., & Billi, A. (2019). The minimum scale of grooving on a recently ruptured limestone fault. *Geophysical Research Letters*, *46*(21), 11878-11885. https://doi.org/10.1029/2019GL084889

81. Pei, L., Hyun, S., Molinari, J.-F., & Robbins, M.O. (2005). Finite element modeling of elasto-plastic contact between rough surfaces. *Journal of the Mechanics and Physics of Solids*, *53*(11), 2385-2409. https://doi.org/10.1016/j.jmps.2005.06.008

82. Perfettini, H., & Molinari, A. (2017). A micromechanical model of rate and state friction: 1. Static and dynamic sliding. *Journal of Geophysical Research: Solid Earth*, *122*(4), 2590-2637. https://doi.org/10.1002/2016JB013302

83. Perrin, G., Rice, J.R., & Zheng, G. (1995). Self-healing slip pulse on a frictional surface. *Journal of the Mechanics and Physics of Solids*, *43*(9), 1461-1495. https://doi.org/10.1016/0022-5096(95)00036-I

84. Persson, B.N.J. (2001). Theory of rubber friction and contact mechanics. *The Journal of Chemical Physics*, *115*, 3840. https://doi.org/10.1063/1.1388626

85. Persson, B.N.J. (2006). Contact mechanics for randomly rough surfaces. *Surface Science Reports*, *61*(4), 201-227. https://doi.org/10.1016/j.surfrep.2006.04.001

86. Proietti, A., Bystricky, M., Guignard, J., Bejina, F., & Crichton, W. (2016). Effect of pressure on the strength of olivine at room temperature. *Physics of Earth and Planetary Interiors*, *259*, 34-44. https://doi.org/10.1016/j.pepi.2016.08.004

87. Putelat, T., Dawes, J.H.P., & Willis, J.R. (2010). Regimes of frictional sliding of a spring-block system. *Journal of the Mechanics and Physics of Solids*, *58*(1), 27-53. https://doi.org/10.1016/j.jmps.2009.09.001

88. Qin, Q., & Bassani, J.L. (1992). Non-associated plastic flow in single crystals. *Journal of the Mechanics and Physics of Solids*, *40*(4), 835-862. https://doi.org/10.1016/0022-5096(92)90006-n

89. Renard, F., Voisin, C., Marsan, D., & Schmittbuhl, J. (2006). High resolution 3d laser scanner measurements of a strike-slip fault quantify its morphological anisotropy at all scales. *Geophysical Research Letters*, *33*(4), https://doi.org/10.1029/2005GL025038

90. Rice, J.R., Lapusta, N., & Ranjith, K. (2001). Rate and state dependent friction and the stability of sliding between elastically deformable solids. *Journal of the Mechanics and Physics of Solids*, *49*(9), 1865-1898. https://doi.org/10.1016/S0022-5096(01)00042-4

91. Rice, J.R. (1983). Constitutive relations for fault slip and earthquake instabilities. *Instabilities in Continuous Media*, 443-475, https://doi.org/10.1007/978-3-0348-6608-8_7

92. Rice, J.R., & Ruina, A.L. (1983). Stability of steady friction slipping. *Journal of Applied Mechanics*, *50*, 343-349. https://doi.org/10.1115/1.3167042

93. Rubin, A.M., (2008). Episodic slow slip events and rate-and-state friction. *Journal of Geophysical Research: Solid Earth*, *113*(B11), https://doi.org/10.1029/2008JB005642

94. Rubin, A.M., & Ampuero, J.-P. (2005). Earthquake nucleation on (aging) rate and state faults. *Journal of Geophysical Research: Solid Earth*, *110*(B11), https://doi.org/10.1029/2005JB003686

95. Ruina, A. (1981). Friction laws and instabilities: A quasistatic analysis of some dry frictional behavior. Ph.D. Dissertation, Brown University, https://www.proquest.com/dissertations-theses/friction-laws-instabilities-quasistatic-analysis/docview/303005988/se-2?accountid=14523

96. Ruina, A. (1983). Slip instability and state variable friction laws. *Journal of Geophysical Research: Solid Earth*, *88*(B12), 10359- 10370, https://doi.org/10.1029/JB088iB12p10359

97. Safaei, M., Lee, M.-G., Zang, S.-L., & De Waele, W. (2014). An evolutionary anisotropic model for sheet metals based on non-associated flow rule approach. *Computational Materials Science*, *81*, 15-29. https://doi.org/10.1016/j.commatsci.2013.05.035

98. Scholz, C.H., (2002). *The Mechanics of Earthquakes and Faulting*. Cambridge University Press.

99. Sevillano, J.G., van Houtte, P., & Aernoudt, E. (1980). Large strain work hardening and textures. *Progress in Materials Science*, *25*(2-4), 69-134. https://doi.org/10.1016/0079-6425(80)90001-8

100. Shibazaki, B., & Iio, Y. (2003). On the physical mechanism of silent slip events along the deeper part of the seismogenic zone. *Geophysical Research Letters*, *30*(9), https://doi.org/10.1029/2003GL017047

101. Sinclair, C.W., Poole, W.J., & Brechet, Y. (2006). A model for the grain size dependent work hardening of copper. *Scripta Materialia*, *55*(8), 739-743. https://doi.org/10.1016/j.scriptamat.2006.05.018

102. Sleep, N.H. (2006). Real contacts and evolution laws for rate and state friction. *Geochemistry, Geophysics, Geosystems*, *7*(8), https://doi.org/10.1029/2005GC001187

103. Stesky, R.M. (1978). Rock friction-effect of confining pressure, temperature, and pore pressure. *Pure and Applied Geophysics*, *116*, 690-704. https://doi.org/10.1007/BF00876532

104. Stoughton, T.B., & Yoon, J.W. (2009). Anisotropic hardening and non-associated flow in proportional loading of sheet metals. *International Journal of Plasticity*, *25*(9), 1777-1817. https://doi.org/10.1016/j.ijplas.2009.02.003

105. Taylor, G.I. (1934). The mechanism of plastic deformation of crystals. Part I.- Theoretical. *Proceedings of the Royal Society A*, *145*(855). https://doi.org/10.1098/rspa.1934.0106

106. Thom, C.A., Brodsky, E.E., Carpick, R.W., Pharr, G.M., Oliver, W.C., & Goldsby, D.L. (2017). Nanoscale roughness of natural fault surfaces controlled by scale-dependent yield strength. *Geophysical Research Letters*, *44*(18), 9299-9307. https://doi.org/10.1002/2017GL074663

107. Thom, C.A., Carpick, R.W., & Goldsby, D.L. (2018). Constraints on the physical mechanism of frictional aging from nanoindentation. *Geophysical Research Letters*, *45*(24), 13,306-13,311. https://doi.org/10.1029/2018GL080561

108. Thom, C.A., & Goldsby, D.L. (2019). Nanoindentation studies of plasticity and dislocation creep in halite. *Geosciences*, *9*(2), 79. https://doi.org/10.3390/geosciences9020079

109. Thom, C.A., Hansen, L.N., Breithaupt, T., Goldsby, D.L., & Kumamoto, K.M. (2021). Backstresses from dislocation interactions quantified by nanoindentation load-drop experiments. https://eartharxiv.org/repository/view/1823/

110. Tian, K., Goldsby, D.L., & Carpick, R.W. (2018). Rate and state friction relation for nanoscale contacts: Thermally activated Prandtl-Tomlinson model with chemical aging. *Physical Review Letters*, *120*, 186101. https://doi.org/10.1103/PhysRevLett.120.186101

111. Tiwari, A., Almqvist, A., & Persson, B.N.J. (2020). Plastic deformation of rough metallic surfaces. *Tribology Letters*, *68*, 129. https://doi.org/10.1007/s11249-020-01368-9

112. Toriumi, M., & Karato, S.-I. (1978). Experimental studies on the recovery processes of deformed olivines and the mechanical state of the upper mantle. *Tectonophysics*, *49*(1), 79-95. https://doi.org/10.1016/0040-1951(78)90098-7

113. Turcotte, D.L., & Schubert, G. (2014). *Geodynamics*. Cambridge University Press.

114. van den Ende, M.P.A., Chen, J., Ampuero, J.-P., & Niemeijer, A.R. (2018). A comparison between rate-and-state friction and microphysical models, based on numerical simulations of fault slip. *Tectonophysics*, *733*, 273-295. https://doi.org/10.1016/j.tecto.2017.11.040

115. Venugopalan, S.P., Irani, N., & Nicola, L. (2019). Plastic contact of self-affine surfaces: Persson's theory versus discrete dislocation plasticity. *Journal of the Mechanics and Physics of Solids*, *132*, 103676. https://doi.org/10.1016/j.jmps.2019.07.019

116. Verberne, B.A., van den Ende, M.P.A., Chen, J., Niemeijer, A.R., & Spiers, C.J. (2020). The physics of fault friction: insights from experiments on simulated gouges at low shearing velocities. *Solid Earth*, *11*, 2075-2095. https://doi.org/10.5194/se-11-2075-2020

117. Wallis, D., Hansen, L.N., Kumamoto, K.M., Thom, C.A., Plümper, O., Ohl, M., et al. (2020). Dislocation interactions during low-temperature plasticity of olivine and their impact on the evolution of lithospheric strength. *Earth and Planetary Science Letters*, *543*, 116349. https://doi.org/10.1016/j.epsl.2020.116349

118. Wallis, D., Hansen, L.N., Wilkinson, A.J., & Lebensohn, R.A. (2021). Dislocation interactions in olivine control postseismic creep of the upper mantle. *Nature Communications*, *12*, 3496. https://doi.org/10.1038/s41467-021-23633-8

119. Zienkiewicz, O.C., Hupheson, C., & Lewis, R.W. (1975). Associated and non-associated visco-plasticity and plastiticty in soil mechanics. *Geotechnique*, *25*(4), 671-689. https://doi.org/10.1680/geot.1975.25.4.671